

HOG-Diff: Higher-Order Guided Diffusion for Graph Generation

Yiming Huang¹ Tolga Birdal¹

Abstract

Graph generation is a critical yet challenging task as empirical analyses require a deep understanding of complex, non-Euclidean structures. Although diffusion models have recently made significant achievements in graph generation, these models typically adapt from the frameworks designed for image generation, making them ill-suited for capturing the topological properties of graphs. In this work, we propose a novel Higher-order Guided Diffusion (HOG-Diff) model that follows a coarse-to-fine generation curriculum and is guided by higher-order information, enabling the progressive generation of plausible graphs with inherent topological structures. We further prove that our model exhibits a stronger theoretical guarantee than classical diffusion frameworks. Extensive experiments on both molecular and generic graph generation tasks demonstrate that our method consistently outperforms or remains competitive with state-of-the-art baselines. Our code is available at <https://github.com/Yimingh/HOG-Diff>.

1. Introduction

Graphs provide an elegant abstraction for representing complex empirical phenomena by encoding entities as vertices and their relationships as edges, thereby transforming unstructured data into analyzable representations. Modelling the underlying distribution of graph-structured data is a crucial yet challenging task with broad applications, including social network analysis, motion synthesis, drug discovery, protein design, and urban planning (Zhu et al., 2022). The study of graph generation seeks to synthesize graphs that align with the observed distribution and traces back to seminal models of random network models (Erdős et al., 1960; Barabási & Albert, 1999). While these models offer foundational insights, they are often too simplistic to capture the complexity of graph distributions we encounter in practice.

Recently, advances in generative models have leveraged

¹Imperial College London, London, United Kingdom. Correspondence to: Tolga Birdal <t.birdal@imperial.ac.uk>.

Preliminary work.

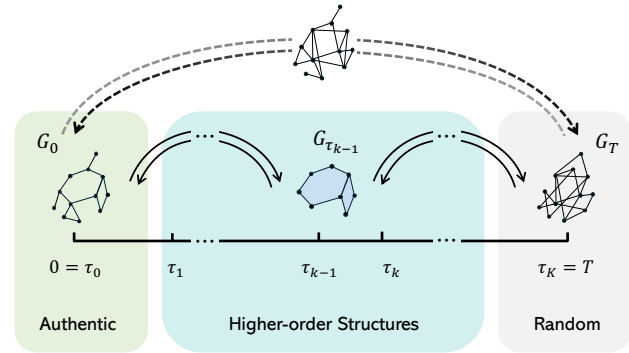


Figure 1. Overview of HOG-Diff. The dashed line above illustrates the classical generation process, where graphs quickly degrade into random structures with uniformly distributed entries. In contrast, as shown in the coloured region below, HOG-Diff adopts a coarse-to-fine generation curriculum based on the diffusion bridge, explicitly learning higher-order structures during intermediate steps with theoretically guaranteed performance.

the power of deep neural networks to significantly improve the ability to learn graph distributions. Notable approaches include models based on recurrent neural networks (RNNs) (You et al., 2018), variational autoencoders (VAEs) (Jin et al., 2018), and generative adversarial networks (GANs) (De Cao & Kipf, 2018; Martinkus et al., 2022). However, the end-to-end structure of these methods makes them hard to train. More recently, diffusion-based models have achieved remarkable success in image generation by learning a model to denoise a noisy sample (Ho et al., 2020; Song et al., 2021). With the advent of diffusion models, their applications on graphs with complex topological structural properties have recently aroused significant scientific interest (Niu et al., 2020; Jo et al., 2022; Vignac et al., 2023).

Despite these advances, existing graph generative models typically inherit the frameworks designed for image generation (Song et al., 2021), which fundamentally limits their ability to capture the intrinsic topological properties of networks. Notably, networks exhibit higher-order structures, such as motifs, simplices, and cells, which capture multi-way interactions and critical topological dependencies beyond pairwise relationships (Battiston et al., 2020; Zeng et al., 2024b; Papamarkou et al., 2024). These structures are vital for representing complex phenomena in domains like molecular graphs, social networks, and protein interactions.

However, current methods are ineffective at modelling the topological properties of higher-order systems since *learning to denoise the noisy samples does not explicitly preserve the intricate structural dependencies required for generating realistic graphs*.

Moreover, the image corrupted by Gaussian noise retains recognizable numerical patterns during the early and middle stages of forward diffusion. By contrast, the graph adjacency matrix quickly degrades into a dense matrix with uniformly distributed entries within a few diffusion steps. In addition, directly applying diffusion-based generative models to graph topology generation by injecting isotropic Gaussian noise to adjacency matrices is harmful as it destroys critical graph properties such as sparsity and connectivity. Lastly, such a framework should ensure equivariance¹, maintaining the learned distribution despite node index permutations, which is essential for robustness and capturing intrinsic graph distribution. Therefore, a graph-friendly diffusion process should also retain meaningful intermediate states and trajectories, avoid inappropriate noise addition, and ensure equivariance.

Motivated by these principles and advances in *topological deep learning* (Hajj et al., 2022; Papamarkou et al., 2024), we propose the **Higher-order Guided Diffusion** (HOG-Diff) framework, illustrated in Fig. 1, to address the gaps in graph generation. HOG-Diff introduces a coarse-to-fine generation curriculum that enhances the model’s ability to capture complex graph properties by preserving higher-order topologies throughout the diffusion process. Specifically, we decompose the graph generation task into manageable sub-tasks, beginning by generating higher-order graph skeletons that capture core structures, which are then refined to include pairwise interactions and finer details, resulting in complete graphs with both topological and semantic fidelity. Additionally, HOG-Diff integrates diffusion bridge and spectral diffusion to ensure effective generation and adherence to the aforementioned graph generation principles. Our theoretical analysis reveals that HOG-Diff converges more rapidly in score matching and achieves sharper reconstruction error bounds than classical approaches, offering strong theoretical support for the proposed framework. Furthermore, our framework promises to enhance interpretability by enabling the analysis of different topological guides’ performance in the generation process. The contributions of this paper are threefold:

- **Algorithmic:** we introduce a coarse-to-fine graph generation curriculum guided by higher-order topological information using the OU diffusion bridge.
- **Theoretical:** our analysis reveals that HOG-Diff achieves faster convergence during score-matching and a sharper reconstruction error bound compared to classical methods.

¹invariance as a particular special case

- **Experimental:** extensive evaluations show that HOG-Diff achieves state-of-the-art graph generation performance across various datasets, highlighting the functional importance of topological guidance.

2. Preliminaries

Higher-order Networks. Graphs are elegant and useful abstractions for various empirical objects; typically, they can be represented as $G \triangleq (V, E, X)$. Here, V denote the node set, $E \subseteq V \times V$, and X denotes the nodes feature matrix. However, many empirical systems exhibit group interactions that extend beyond simple pairwise relationships (Battiston et al., 2020). To capture these complex interactions, higher-order networks—such as hypergraphs, simplicial complexes, and cell complexes—offer more expressive alternatives by capturing higher-order interactions among entities (Papamarkou et al., 2024). Among these, cell complexes are fundamental in algebraic topology, offering a flexible generalization of pairwise graphs (Hatcher, 2001).

Definition 2.1 (Regular cell complex). A regular cell complex is a topological space \mathcal{S} with a partition into subspaces (cells) $\{x_\alpha\}_{\alpha \in P_{\mathcal{S}}}$, where $P_{\mathcal{S}}$ is an index set, satisfying the following conditions:

1. For any $x \in \mathcal{S}$, every sufficiently small neighborhood of x intersects finitely many cells.
2. For each cell x_α , the boundary ∂x_α is a union of finitely many cells, each having dimension less than that of x_α .
3. Each cell x_α is homeomorphic to \mathbb{R}^{n_α} , where n_α is dimension of x_α .
4. (Regularity) For every $\alpha \in P_{\mathcal{S}}$, there exists a homeomorphism ϕ of a closed ball $\mathbb{B}^{n_\alpha} \subset \mathbb{R}^{n_\alpha}$ to the closure $\overline{x_\alpha}$ such that the restriction of ϕ to the interior of the ball is a homeomorphism onto x_α .

From this definition, we can derive that \mathcal{S} is the union of the interiors of all cells, *i.e.*, $\mathcal{S} = \cup_{\alpha \in P_{\mathcal{S}}} \text{int}(x_\alpha)$, where $\text{int}(x_\alpha)$ denotes the interior of the cell x_α . Intuitively, a cell complex can be constructed hierarchically through a gluing procedure. It begins with a set of vertices (0-cells), to which edges (1-cells) are attached by gluing the endpoints of closed line segments, thereby forming a graph. This process can be extended by taking a two-dimensional closed disk and gluing its boundary (*i.e.*, a circle) to a simple cycle in the graph. While we typically focus on dimensions up to two, this framework can be further generalized by gluing the boundary of n -dimensional balls to specific $(n - 1)$ -cells in the complex. In this work, we also utilize simplicial complexes (SCs), a simpler and more restrictive subclass where 2-cells are limited to triangle shapes. A further introduction to higher-order networks can be found in App. B.

Score-based Diffusion Models. A fundamental goal of generative models is to produce plausible samples from an unknown target data distribution $p(\mathbf{x}_0)$. Score-based diffusion

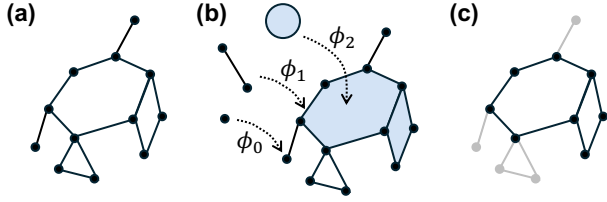


Figure 2. Visualization of Cell Complex Transformations. (a) An example graph. (b) Cell complex representation with corresponding homeomorphisms to closed balls for three example cells. (c) Black elements represent high-order structures extracted from the original graph through 2-cell filtering, while those in grey denote corresponding peripheral structures.

models (Song & Ermon, 2019; Song et al., 2021) achieve this by progressively corrupting the authentic data with noise and subsequently training a neural network to reverse this corruption process, thereby generating meaningful data from a tractable prior distribution, *i.e.*, $\mathbf{x}_{generated} \sim p(\mathbf{x}_0)$.

Specifically, the time-dependent forward process of the diffusion model can be described by the following stochastic differential equation (SDE):

$$d\mathbf{x}_t = \mathbf{f}_t(\mathbf{x}_t) dt + g_t d\mathbf{w}_t, \quad (1)$$

where $\mathbf{f}_t : \mathbb{R}^n \rightarrow \mathbb{R}^n$ is a vector-valued drift function, $g_t : [0, T] \rightarrow \mathbb{R}$ is a scalar diffusion coefficient, and \mathbf{w}_t represents a Wiener process. Typically, $p(\mathbf{x}_0)$ evolves over time t from 0 to a sufficiently large T into $p(\mathbf{x}_T)$ through the SDE, such that $p(\mathbf{x}_T)$ will approximate a tractable prior distribution, for example, a standard Gaussian distribution.

Starting from time T , $p(\mathbf{x}_T)$ can be progressively transformed back to $p(\mathbf{x}_0)$ by following the trajectory of the following reverse SDE (Anderson, 1982):

$$d\mathbf{x}_t = [\mathbf{f}_t(\mathbf{x}_t) - \underbrace{g_t^2 \nabla_{\mathbf{x}_t} \log p_t(\mathbf{x}_t)}_{\text{score function}}] dt + g_t d\bar{\mathbf{w}}, \quad (2)$$

where $p_t(\cdot)$ denote the probability density function of \mathbf{x}_t and $\bar{\mathbf{w}}$ is a reverse-time Wiener process. The score function is typically parameterized as a neural network $\mathbf{s}_\theta(\mathbf{x}_t, t)$ and trained using the score-matching technique as the loss function (Vincent, 2011):

$$\begin{aligned} \ell(\theta) &\triangleq \mathbb{E}_{t, \mathbf{x}_t} \left[\omega(t) \|\mathbf{s}_\theta(\mathbf{x}_t, t) - \nabla_{\mathbf{x}_t} \log p_t(\mathbf{x}_t)\|^2 \right] \\ &\propto \mathbb{E}_{t, \mathbf{x}_0, \mathbf{x}_t} \left[\omega(t) \|\mathbf{s}_\theta(\mathbf{x}_t, t) - \nabla_{\mathbf{x}_t} \log p_t(\mathbf{x}_t | \mathbf{x}_0)\|^2 \right], \end{aligned} \quad (3)$$

where $\omega(t)$ is a weighting function, and the second expression is more commonly used as the conditional probability $p_t(\mathbf{x}_t | \mathbf{x}_0)$ is generally accessible. Ultimately, the generation process is complete by first sampling \mathbf{x}_T from a tractable prior distribution $p(\mathbf{x}_T) \approx p_{prior}(\mathbf{x})$ and then generating \mathbf{x}_0 by numerically solving Eq. (2).

Doob’s h -transform. Doob’s h -transform is a mathematical framework widely used to modify stochastic processes,

enabling the process to satisfy specific terminal conditions. By introducing an h -function into the drift term of an SDE, this technique ensures that the process transitions to a predefined endpoint while preserving the underlying probabilistic structure. Specifically, given the SDE in Eq. (1), Doob’s h -transform alters the SDE to include an additional drift term, ensuring that the process reaches a fixed terminal point $t = T$. The modified SDE is expressed as:

$$d\mathbf{x}_t = [\mathbf{f}_t(\mathbf{x}_t) + g_t^2 \mathbf{h}(\mathbf{x}_t, t, \mathbf{x}_T, T)] dt + g_t d\mathbf{w}_t, \quad (4)$$

where $\mathbf{h}(\mathbf{x}_t, t, \mathbf{x}_T, T) = \nabla_{\mathbf{x}_t} \log p(\mathbf{x}_T | \mathbf{x}_t)$. Crucially, the construction guarantees the conditional density satisfies $p(\mathbf{x}_t | \mathbf{x}_0, \mathbf{x}_T) = 1$ at $t = T$, ensuring that SDE terminates at the specified endpoint \mathbf{x}_T .

3. Higher-order Guided Diffusion Model

We now present our *Higher-order Guided Diffusion* (HOG-Diff) model, which enhances graph generation by exploiting higher-order structures. We begin by detailing a coarse-to-fine generation curriculum that incrementally constructs graphs, followed by the introduction of three essential supporting techniques: the diffusion bridge, spectral diffusion, and a denoising model, respectively. Finally, we provide theoretical evidence validating the efficacy of HOG-Diff.

Coarse-to-fine Generation. We draw inspiration from curriculum learning, a paradigm that mimics the human learning process by systematically organizing data in a progression from simple to complex (Soviany et al., 2022). Likely, an ideal graph generation curriculum should be a composition of multiple easy-to-learn and meaningful intermediate steps. Additionally, higher-order structures encapsulate rich structural properties beyond pairwise interactions that are crucial for various empirical systems (Huang et al., 2024). As a graph-friendly generation framework, HOG-Diff incorporates higher-order structures during the intermediate stages of forward diffusion and reverse generative processes, thereby realizing a coarse-to-fine generation curriculum.

To implement our coarse-to-fine generation curriculum, we introduce a key operation termed cell complex filtering (CCF). As illustrated in Fig. 2, CCF generates an intermediate state of a graph by pruning nodes and edges that do not belong to a given cell complex.

Definition 3.1 (Cell complex filtering). Given a graph $G = (\mathbf{V}, \mathbf{E})$ and its associated cell complex \mathcal{S} , the cell complex filtering operation produces a filtered graph $G' = (\mathbf{V}', \mathbf{E}')$ where $\mathbf{V}' = \{v \in \mathbf{V} \mid \exists x_\alpha \in \mathcal{S} : v \in x_\alpha\}$, and $\mathbf{E}' = \{(u, v) \in \mathbf{E} \mid \exists x_\alpha \in \mathcal{S} : u, v \in x_\alpha\}$.

This filtering operation is a pivotal step in decomposing the graph generation task into manageable sub-tasks, with the filtered results serving as natural intermediaries in hierarchical graph generation. The overall framework of our

proposed framework is depicted in Fig. 1. Specifically, the forward and reverse diffusion processes in HOG-Diff are divided into K hierarchical time windows, denoted as $\{[\tau_{k-1}, \tau_k]\}_{k=1}^K$, where $0 = \tau_0 < \dots < \tau_{k-1} < \tau_k < \dots < \tau_K = T$. Our sequential generation progressively denoises the higher-order skeletons. First, we generate coarse-grained higher-order skeletons, and subsequently refine them into finer pairwise relationships, simplifying the task of capturing complex graph distributions. This coarse-to-fine approach inherently aligns with the hierarchical nature of many real-world graphs, enabling smoother training and improved sampling performance.

Formally, our generation process factorizes the joint distribution of the final graph \mathbf{G}_0 into a product of conditional distributions across these time windows:

$$p(\mathbf{G}_0) = p(\mathbf{G}_0 | \mathbf{G}_{\tau_1}) p(\mathbf{G}_{\tau_1} | \mathbf{G}_{\tau_2}) \dots p(\mathbf{G}_{\tau_{K-1}} | \mathbf{G}_T). \quad (5)$$

Here, intermediate states $\mathbf{G}_{\tau_1}, \mathbf{G}_{\tau_2}, \dots, \mathbf{G}_{\tau_{K-1}}$ represents different levels of cell filtering results of the corresponding graph. Our approach aligns intermediate stages of the diffusion process with realistic graph representations, and the ordering reflects a coarse-to-fine generation process.

The forward process introduces noise in a stepwise manner while preserving intermediate structural information. During each time window $[\tau_{k-1}, \tau_k]$, the evolution of the graph is governed by the following forward SDE:

$$d\mathbf{G}_t^{(k)} = \mathbf{f}_{k,t}(\mathbf{G}_t^{(k)}) dt + g_{k,t} d\mathbf{W}_t, t \in [\tau_{k-1}, \tau_k]. \quad (6)$$

Reversing this process enables the model to generate authentic samples with desirable higher-order information. The reverse-time SDE corresponds to Eq. (6) is as follows:

$$d\mathbf{G}_t^{(k)} = \left[\mathbf{f}_{k,t}(\mathbf{G}_t^{(k)}) - g_{k,t}^2 \nabla_{\mathbf{G}_t^{(k)}} \log p_t(\mathbf{G}_t^{(k)}) \right] d\bar{t} + g_{k,t} d\bar{\mathbf{W}}_t. \quad (7)$$

Instead of using higher-order information as a direct condition, HOG-Diff employs it to guide the generation process through multiple steps. This strategy allows the model to incrementally build complex graph structures while maintaining meaningful structural integrity at each stage. Moreover, integrating higher-order structures into graph generative models improves interpretability by allowing analysis of their significance in shaping the graph's properties.

Diffusion Bridge Process. We realize the guided diffusion based on the generalized Ornstein-Uhlenbeck (GOU) process (Ahmad, 1988; Luo et al., 2023b), a stationary Gaussian-Markov process characterized by its mean-reverting property. Over time, the marginal distribution of the GOU process stabilizes around a fixed mean and variance, making it well-suited for stochastic modelling with

terminal constraints. The GOU process \mathbb{Q} is governed by the following SDE:

$$\mathbb{Q} : d\mathbf{G}_t = \theta_t(\boldsymbol{\mu} - \mathbf{G}_t)dt + g_t(\mathbf{G}_t)d\mathbf{W}_t, \quad (8)$$

where $\boldsymbol{\mu} = \mathbf{G}_{\tau_k}$ is the target terminal state, θ_t denotes a scalar drift coefficient and g_t represents the diffusion coefficient. To ensure the process remains analytically tractable, θ_t and g_t are constrained by the relationship $g_t^2/\theta_t = 2\sigma^2$ (Luo et al., 2023b), where σ^2 is a given constant scalar. Under these conditions, its transition probability admits a closed-form solution:

$$p(\mathbf{G}_t | \mathbf{G}_s) = \mathcal{N}(\mathbf{m}_{s:t}, v_{s:t}^2 \mathbf{I}) \\ = \mathcal{N}\left(\boldsymbol{\mu} + (\mathbf{G}_s - \boldsymbol{\mu}) e^{-\bar{\theta}_{s:t}}, \sigma^2(1 - e^{-2\bar{\theta}_{s:t}})\mathbf{I}\right). \quad (9)$$

Here, $\bar{\theta}_{s:t} = \int_s^t \theta_z dz$, and for notional simplicity, $\bar{\theta}_{0:t}$ is replaced by θ_t when $s = 0$. At time t progress, $p(\mathbf{G}_t)$ gradually approaches a Gaussian distribution characterized by mean $\boldsymbol{\mu}$ and variance σ^2 , indicating that the GOU process exhibits the mean-reverting property.

The Doob's h -transform can modify an SDE such that it passes through a specified endpoint. When applied to the GOU process, this eliminates variance in the terminal state, driving the diffusion process toward a Dirac distribution centered at \mathbf{G}_{τ_k} (Heng et al., 2021; Yue et al., 2024).

Proposition 3.2. *Let \mathbf{G}_t evolve according to the generalized OU process in Eq. (8), subject to the terminal conditional $\boldsymbol{\mu} = \mathbf{G}_{\tau_k}$. The conditional marginal distribution $p(\mathbf{G}_t | \mathbf{G}_{\tau_k})$ then evolves according to the following SDE:*

$$d\mathbf{G}_t = \theta_t \left(1 + \frac{2}{e^{2\bar{\theta}_{t:\tau_k}} - 1} \right) (\mathbf{G}_{\tau_k} - \mathbf{G}_t) dt + g_{k,t} d\mathbf{W}_t.$$

The conditional transition probability $p(\mathbf{G}_t | \mathbf{G}_{\tau_{k-1}}, \mathbf{G}_{\tau_k})$ has analytical form as follows:

$$p(\mathbf{G}_t | \mathbf{G}_{\tau_{k-1}}, \mathbf{G}_{\tau_k}) = \mathcal{N}(\bar{\mathbf{m}}_t, \bar{v}_t^2 \mathbf{I}), \\ \bar{\mathbf{m}}_t = \mathbf{G}_{\tau_k} + (\mathbf{G}_{\tau_{k-1}} - \mathbf{G}_{\tau_k}) e^{-\bar{\theta}_{\tau_{k-1}:t}} \frac{v_{t:\tau_k}^2}{v_{\tau_{k-1}:t}^2}, \quad (10) \\ \bar{v}_t^2 = v_{\tau_{k-1}:t}^2 v_{t:\tau_k}^2 / v_{\tau_{k-1}:t}^2.$$

Here, $\bar{\theta}_{a:b} = \int_a^b \theta_s ds$, and $v_{a:b} = \sigma^2(1 - e^{-2\bar{\theta}_{a:b}})$.

We can directly use the closed-form solution in Prop. 3.2 for one-step forward sampling without performing multi-step forward iteration using the SDE. The reverse-time dynamics of the conditioned process can be derived using the theory of SDEs and take the following form:

$$d\mathbf{G}_t = \left[\mathbf{f}_{k,t}(\mathbf{G}_t) - g_{k,t}^2 \nabla_{\mathbf{G}_t} \log p(\mathbf{G}_t | \mathbf{G}_{\tau_k}) \right] d\bar{t} + g_{k,t} d\bar{\mathbf{W}}_t,$$

where $\mathbf{f}_{k,t}(\mathbf{G}_t) = \theta_t \left(1 + \frac{2}{e^{2\bar{\theta}_{t:\tau_k}} - 1} \right) (\mathbf{G}_{\tau_k} - \mathbf{G}_t)$.

Spectral Diffusion. Generating graph adjacency matrices presents several significant challenges. Firstly, the non-uniqueness of graph representations implies that a graph with n vertices can be equivalently modelled by up to $n!$ distinct adjacency matrices. This ambiguity requires a generative model to assign probabilities uniformly across all equivalent adjacencies to accurately capture the graph’s inherent symmetry. Additionally, unlike densely distributed image data, graphs typically follow a Pareto distribution and exhibit sparsity (Ghavasieh & De Domenico, 2024), so that adjacency score functions lie on a low-dimensional manifold. Consequently, noise injected into out-of-support regions of the full adjacency space severely degrades the signal-to-noise ratio, impairing the training of the score-matching process. Even for densely connected graphs, isotropic noise distorts global message-passing patterns by encouraging message-passing on sparsely connected regions. Moreover, the adjacency matrix scales quadratically with the number of nodes, making the direct generation of adjacency matrices computationally prohibitive for large-scale graphs.

To address these challenges, inspired by Martinkus et al. (2022); Luo et al. (2023a), we introduce noise in the eigenvalue domain of the graph Laplacian matrix $L = D - A$, instead of the adjacency matrix A , where D denotes the diagonal degree matrix. As a symmetric positive semi-definite matrix, the graph Laplacian can be diagonalized as $L = U\Lambda U^\top$. Here, the orthogonal matrix $U = [u_1, \dots, u_n]$ comprises the eigenvectors, and the diagonal matrix $\Lambda = \text{diag}(\lambda_1, \dots, \lambda_n)$ holds the corresponding eigenvalues. The relationship between the Laplacian spectrum and the graph’s topology has been extensively explored (Chung, 1997). For instance, the low-frequency components of the spectrum capture the global structural properties such as connectivity and clustering, whereas the high-frequency components are crucial for reconstructing local connectivity patterns. Therefore, the target graph distribution $p(\mathbf{G}_0)$ represents a joint distribution of \mathbf{X}_0 and Λ_0 , exploiting the permutation invariance and structural robustness of the Laplacian spectrum. Consequently, we split the reverse-time SDE into two parts that share drift and diffusion coefficients as

$$\begin{cases} d\mathbf{X}_t = [\mathbf{f}_{k,t}(\mathbf{X}_t) - g_{k,t}^2 \nabla_{\mathbf{X}} \log p_t(\mathbf{G}_t | \mathbf{G}_{\tau_k})] d\bar{t} + g_{k,t} d\bar{\mathbf{W}}_t^1 \\ d\Lambda_t = [\mathbf{f}_{k,t}(\Lambda_t) - g_{k,t}^2 \nabla_{\Lambda} \log p_t(\mathbf{G}_t | \mathbf{G}_{\tau_k})] d\bar{t} + g_{k,t} d\bar{\mathbf{W}}_t^2 \end{cases}$$

Here, the superscript of $\mathbf{X}_t^{(k)}$ and $\Lambda_t^{(k)}$ are dropped for simplicity, and $\mathbf{f}_{k,t}$ is determined according to Prop. 3.2.

To approximate the score functions $\nabla_{\mathbf{X}_t} \log p_t(\mathbf{G}_t | \mathbf{G}_{\tau_k})$ and $\nabla_{\Lambda_t} \log p_t(\mathbf{G}_t | \mathbf{G}_{\tau_k})$, we employ a neural network $\mathbf{s}_{\theta}^{(k)}(\mathbf{G}_t, \mathbf{G}_{\tau_k}, t)$, composed of a node ($\mathbf{s}_{\theta, \mathbf{X}}^{(k)}(\mathbf{G}_t, \mathbf{G}_{\tau_k}, t)$) and a spectrum ($\mathbf{s}_{\theta, \Lambda}^{(k)}(\mathbf{G}_t, \mathbf{G}_{\tau_k}, t)$) output, respectively. The

model is optimized by minimizing the loss function:

$$\begin{aligned} \ell^{(k)}(\theta) = & \mathbb{E}_{t, \mathbf{G}_t, \mathbf{G}_{\tau_{k-1}}, \mathbf{G}_{\tau_k}} \{ \omega(t) [c_1 \|\mathbf{s}_{\theta, \mathbf{X}}^{(k)} - \nabla_{\mathbf{X}} \log p_t(\mathbf{G}_t | \mathbf{G}_{\tau_k})\|_2^2 \\ & + c_2 \|\mathbf{s}_{\theta, \Lambda}^{(k)} - \nabla_{\Lambda} \log p_t(\mathbf{G}_t | \mathbf{G}_{\tau_k})\|_2^2] \}, \end{aligned} \quad (11)$$

where $\omega(t)$ is a positive weighting function, and c_1, c_2 controls the relative importance of vertices and spectrum. The training procedure is detailed in Alg. 1 in the Appendix.

We sample $(\mathbf{X}_{\tau_K}, \Lambda_{\tau_K})$ from the prior distribution and uniformly sample \mathbf{U}_0 from the observed eigenvector matrices. The generation process involves multi-step diffusion to produce samples $(\hat{\mathbf{X}}_{\tau_{K-1}}, \hat{\Lambda}_{\tau_{K-1}}), \dots, (\hat{\mathbf{X}}_{\tau_1}, \hat{\Lambda}_{\tau_1}), (\hat{\mathbf{X}}_0, \hat{\Lambda}_0)$ in sequence by reversing the diffusion bridge, where the end-point of one generation step serves as the starting point for the next. Finally, plausible samples with higher-order structures $\hat{\mathbf{G}}_0 = (\hat{\mathbf{X}}_0, \hat{\Lambda}_0 = \mathbf{U}_0 \hat{\Lambda}_0 \mathbf{U}_0^\top)$ can be reconstructed. The complete sampling procedure is outlined in Alg. 2 within the Appendix.

Denoising Network Architecture. We design a neural network $\mathbf{s}_{\theta}^{(k)}(\mathbf{G}_t, \mathbf{G}_{\tau_k}, t)$ to estimate score functions in Eq. (11). Standard graph neural networks designed for classical tasks such as graph classification and link prediction may be inappropriate for graph distribution learning due to the immediate real-number graph states and the complicated requirements. For example, an effective model for molecular graph generation should capture local node-edge dependence for chemical valency rules and attempt to recover global graph patterns like edge sparsity, frequent ring subgraphs, and atom-type distribution.

To achieve this, we introduce a unified denoising network that explicitly integrates node and spectral representations. As illustrated in Fig. 6 of Appendix, the network comprises two different graph processing modules: a standard graph convolution network (GCN) (Kipf & Welling, 2017) for local feature aggregation and a graph transformer network (ATTN) (Dwivedi & Bresson, 2021; Vignac et al., 2023) for global information extraction. The outputs of these modules are fused with time information through a Feature-wise Linear Modulation (FiLM) layer (Perez et al., 2018). The resulting representations are concatenated to form a unified hidden embedding. This hidden embedding is further processed through separate multilayer perceptrons (MLPs) to produce predictions for $\nabla_{\mathbf{X}} \log p(\mathbf{G}_t | \mathbf{G}_{\tau_k})$ and $\nabla_{\Lambda} \log p(\mathbf{G}_t | \mathbf{G}_{\tau_k})$, respectively. It is worth noting that our graph noise prediction model is permutation equivalent as each component of our model avoids any node ordering-dependent operations. Our model is detailed in App. D.1.

Theoretical Analysis. In the following, we provide supportive theoretical evidence for the efficacy of HOG-Diff, demonstrating that the proposed framework achieves faster convergence in score-matching and tighter reconstruction error bounds compared to standard graph diffusion works.

Table 1. Comparison of different methods based on molecular datasets. The best results for the first three metrics are highlighted in bold.

Methods	QM9						ZINC250k					
	NSPDK↓	FCD↓	Val. w/o corr.↑	Val.↑	Uni.↑	Nov.↑	NSPDK ↓	FCD ↓	Val. w/o corr.↑	Val.↑	Uni.↑	Nov.↑
GraphAF	0.020	5.268	67.00	100.00	94.51	88.83	0.044	16.289	68.00	100.00	99.10	100.00
GraphAF+FC	0.021	5.625	74.43	100.00	86.59	89.57	0.044	16.023	68.47	100.00	98.64	99.99
GraphDF	0.063	10.816	82.67	100.00	97.62	98.10	0.176	34.202	89.03	100.00	99.16	99.99
GraphDF+FC	0.064	10.928	93.88	100.00	98.32	98.54	0.177	33.546	90.61	100.00	99.63	100.00
MoFlow	0.017	4.467	91.36	100.00	98.65	94.72	0.046	20.931	63.11	100.00	99.99	99.99
EDP-GNN	0.005	2.680	47.52	100.00	99.25	86.58	0.049	16.737	82.97	100.00	99.79	99.99
GraphEBM	0.003	6.143	8.22	100.00	99.25	85.48	0.212	35.471	5.29	99.96	98.79	99.99
GDSS	0.003	2.900	95.72	100.00	98.46	86.27	0.019	14.656	97.01	100.00	99.64	100.00
DiGress	0.0005	0.360	99.00	100.00	96.66	33.40	0.082	23.060	91.02	100.00	81.23	100.00
HOG-Diff	0.0003	0.172	98.74	100.00	97.01	75.12	0.001	1.533	98.56	100.00	99.96	99.43

Proposition 3.3 (Informal). Suppose the loss function $\ell^{(k)}(\theta)$ in Eq. (11) is β -smooth and satisfies the μ -PL condition in the ball $B(\theta_0, R)$. Then, the expected loss at the i -th iteration of the training process satisfies:

$$\mathbb{E} \left[\ell^{(k)}(\theta_i) \right] \leq \left(1 - \frac{b\mu^2}{\beta N(\beta N^2 + \mu(b-1))} \right)^i \ell^{(k)}(\theta_0),$$

where N denotes the size of the training dataset, and b is the mini-batch size. Furthermore, it holds that $\beta_{\text{HOG-Diff}} \leq \beta_{\text{classical}}$, implying that the distribution learned by the proposed framework converges to the target distribution faster than classical generative models.

Following Luo et al. (2023a), we define the expected reconstruction error at each generation process as $\mathcal{E}(t) = \mathbb{E} \left\| \tilde{\mathbf{G}}_t - \hat{\mathbf{G}}_t \right\|^2$, where $\tilde{\mathbf{G}}_t$ represents the data reconstructed using the ground truth score $\nabla \log p_t(\cdot)$ and $\hat{\mathbf{G}}_t$ denotes the data reconstructed with the learned score function s_θ . We establish that the reconstruction error in HOG-Diff is bounded more tightly than in classical graph generation models, ensuring superior sample quality.

Proposition 3.4. Under appropriate Lipschitz and boundedness assumptions, the reconstruction error of HOG-Diff satisfies the following bound:

$$\mathcal{E}(0) \leq \alpha(0) \exp \int_0^{\tau_1} \gamma(s) ds, \quad (12)$$

where $\alpha(0) = C^2 \ell^{(1)}(\theta) \int_0^{\tau_1} g_{1,s}^4 ds + C \mathcal{E}(\tau_1) \int_0^{\tau_1} h_{1,s}^2 ds$, $\gamma(s) = C^2 g_{1,s}^4 \|s_\theta(\cdot, s)\|_{\text{lip}}^2 + C \|h_{1,s}\|_{\text{lip}}^2$, and $h_{1,s} = \theta_s \left(1 + \frac{2}{e^{2\theta_s \tau_1} - 1} \right)$. Furthermore, we can derive that the reconstruction error bound of HOG-Diff is sharper than classical graph generation models.

The propositions above rely primarily on mild assumptions, such as smoothness and boundedness, without imposing strict conditions like the target distribution being log-concave or satisfying the log-Sobolev inequality. Their formal statements and detailed proofs are postponed to App. A. We experimentally verify these Propositions in Sec. 4.3.

4. Experiments

We assess HOG-Diff against state-of-the-art baselines for both molecular and generic graph generation. Further ablation studies are conducted to analyze the impact of different topological guides. More details can be found in App. F.

4.1. Molecule Generation

Experimental Setup. To assess the capability of the proposed method in molecular generation, we conduct evaluations on two well-known molecular datasets: QM9 (Ramakrishnan et al., 2014) and ZINC250k (Irwin et al., 2012), and obtain the intermedia higher-order skeletons using the 2-cell complex filtering. We evaluate the quality of 10,000 generated molecules with six metrics as in Jo et al. (2022): Neighborhood Subgraph Pairwise Distance Kernel (NSPDK) MMD (Costa & Grave, 2010), Fréchet ChemNet Distance (FCD) (Preuer et al., 2018), Validity (Val.), Validity without correction (Val. w/o corr.), Uniqueness (Uni.), and Novelty (Nov.) (Jo et al., 2022).

Baselines. We evaluate our model against state-of-the-art molecular generation models, including auto-regressive methods, GraphAF (Shi et al., 2020), and GraphDF (Luo et al., 2021). For a fair comparison, as recommended by Jo et al. (2022), we extend GraphAF and GraphDF to account for formal charges in the molecular generation, termed GraphAF+FC and GraphDF+FC, respectively. We also compare our HOG-Diff with various flow-based and diffusion-based methods, including MoFlow (Zang & Wang, 2020), EDP-GNN (Niu et al., 2020), Graph-EBM (Liu et al., 2021), GDSS (Jo et al., 2022), and DiGress (Vignac et al., 2023).

Sampling Quality. We visualize the molecule generation process in Fig. 3 with more examples deferred to App. G. It can be observed that our model explicitly preserves higher-order structures during the generation process. Tab. 1 indicates that HOG-Diff consistently outperforms both auto-regressive and one-shot models. Notably, the dramatic decrease in NSPDK and FCD implies that HOG-Diff is able

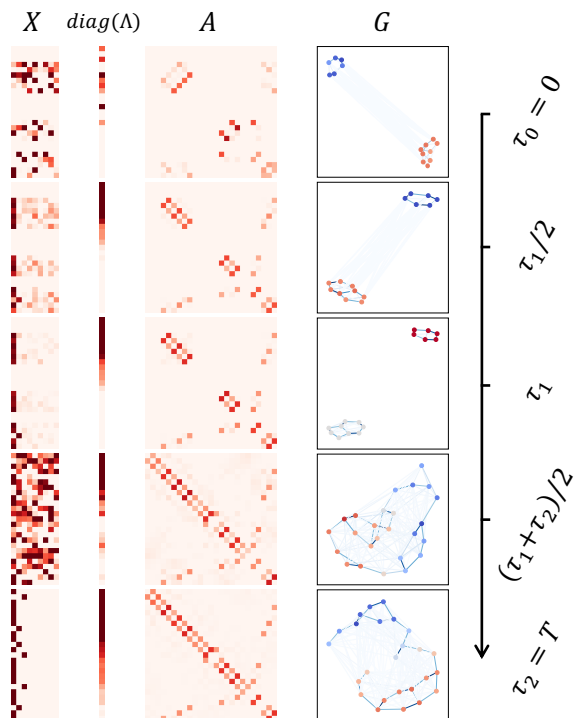


Figure 3. Visualization of molecular graphs at different stages of the reverse generative process. Model trained on Zinc250k.

to generate molecules with data distributions close to those of the real molecules in both the chemical and graph space.

4.2. Generic Graph Generation

Experimental Setup. To display the topology distribution learning ability, we access HOG-Diff over three common generic graph datasets: (1) **Community-small**, containing 100 randomly generated community graphs; (2) **Ego-small**, comprising 200 small ego graphs derived from the Citeseer network dataset; (3) **Enzymes**, featuring 587 protein graphs representing tertiary structures of enzymes from the BRENDA database. Intermediate higher-order skeletons are obtained through 3-simplicial complex filtering, which prunes nodes and edges that do not belong to three-dimensional simplicial complexes. We employ the same train/test split as Jo et al. (2022) for a fair comparison with baselines. Consistent with You et al. (2018), we employ the maximum mean discrepancy (MMD) to quantify the distribution differences across key graph statistics, including degree (**Deg.**), clustering coefficient (**Clus.**), and the number of occurrences of orbits with 4 nodes (**Orbit**). To provide a holistic evaluation, we further calculate the mean MMD across these metrics, which is reported in the **Avg.** column as the overall assessment index. A lower MMD signifies a closer alignment between the generated and evaluation datasets, indicating superior generative performance.

Baselines. We compare our model with prominent autoregressive and one-shot graph generation approaches. Auto-

regressive models sequentially build graphs by adding nodes and edges step-by-step. Benchmarks in this category include DeepGMG (Li et al., 2018), GraphRNN (You et al., 2018), GraphAF (Shi et al., 2020), and GraphDF (Luo et al., 2021). Conversely, one-shot models generate all nodes and edges simultaneously. We include GraphVAE (Simonovsky & Komodakis, 2018), GNF (Liu et al., 2019), GPrinFlowNet (Mo et al., 2024), EDP-GNN (Niu et al., 2020), GDSS (Jo et al., 2022), and DiGress (Vignac et al., 2023).

Sampling Quality. The results in Tab. 2 verify that HOG-Diff is not only suitable for molecular generation but also proficient in generic graph generation. These experiments demonstrate HOG-Diff’s ability to model the intricate interdependencies between nodes and edges effectively.

4.3. Ablations: Topological Guide Analysis

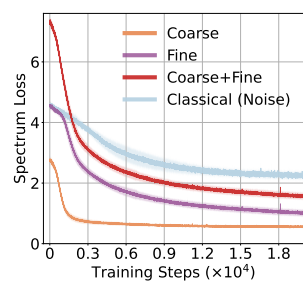
During the experiments, we observe that HOG-Diff exhibits superior performance on complex datasets such as QM9 and Zinc250k, but comparatively modest results on the Ego dataset. Visualizations and statistics in Apps. F and G indicate that Ego contains the fewest higher-order structures among the datasets analyzed, suggesting that the choice of guide plays a pivotal role in the effectiveness of generation. To validate this hypothesis, we conduct further ablations using different types of topological information as guides.

Specifically, we employ three types of guiders: structures derived from 2-cell filtering (**Cell**), peripheral structures obtained by removing cell components (**Peripheral**), and Gaussian random noise (**Noise**). Employing noise as the guide aligns with classical generation models which generate samples by denoising noisy data. Fig. 4 (plot) visualizes how the spectrum loss changes during the training process and demonstrates that training the proposed model converges faster compared to the classical method, which aligns with the theoretical results in Prop. 3.3.

The sampling results in Fig. 4 (table) show that both peripheral and noise guides are inferior compared to using cell structures as the guide, empirically supporting Prop. 3.4. This highlights that certain topological structures, such as cells, are more effective in guiding the generation, likely due to their higher-order connectivity and structural significance. These observations stress the importance of identifying and leveraging proper topological structures as guides, which play a critical role in steering the generative process toward meaningful outputs. Moreover, this property opens up promising avenues for exploring the guide’s potential as a tool to diagnose whether a specific component is integral and essential for the architecture. Furthermore, by systematically analyzing the impact of various guides, we can deepen our understanding of the interplay between structural characteristics and generative performance, thereby advancing the design of more effective graph generative models.

Table 2. Generation performance on generic graph datasets. The best results are highlighted in bold and an underline indicates the second-best result. Hyphen (-) denotes that the results are not provided in the original paper.

Methods	Community-small				Enzymes				Ego-small			
	Deg.↓	Clus.↓	Orbit↓	Avg.↓	Deg.↓	Clus.↓	Orbit↓	Avg.↓	Deg.↓	Clus.↓	Orbit↓	Avg.↓
DeepGMG	0.220	0.950	0.400	0.523	-	-	-	-	0.040	0.100	0.020	0.053
GraphRNN	0.080	0.120	0.040	0.080	0.017	0.062	0.046	0.042	0.090	0.220	0.003	0.104
GraphAF	0.180	0.200	0.020	0.133	1.669	1.283	0.266	1.073	0.030	0.110	0.001	0.047
GraphDF	0.060	0.120	0.030	0.070	1.503	1.061	0.202	0.922	0.040	0.130	0.010	0.060
GraphVAE	0.350	0.980	0.540	0.623	1.369	0.629	0.191	0.730	0.130	0.170	0.050	0.117
GNF	0.200	0.200	0.110	0.170	-	-	-	-	0.030	0.100	0.001	0.044
GPrinFlowNet	<u>0.021</u>	0.068	0.021	<u>0.037</u>	0.021	0.088	0.009	0.039	-	-	-	-
EDP-GNN	0.053	0.144	0.026	0.074	0.023	0.268	0.082	0.124	0.052	0.093	0.007	0.051
GDSS	0.045	0.086	<u>0.007</u>	0.046	0.026	0.061	0.009	0.032	0.021	0.024	0.007	0.017
DiGress	0.047	<u>0.041</u>	0.026	0.038	0.004	0.083	0.002	<u>0.030</u>	0.015	0.029	0.005	0.016
HOG-Diff	0.006	0.022	0.002	0.010	<u>0.011</u>	0.061	<u>0.007</u>	0.027	0.015	<u>0.027</u>	0.004	0.016



Dataset	Guide	NSPDK↓	FCD↓	Val. w/o corr.↑
QM9	Noise	0.0015	0.829	91.52
	Peripheral	0.0009	0.305	97.58
	Cell	0.0003	0.172	98.74
ZINC250k	Noise	0.002	1.665	96.78
	Peripheral	0.002	1.541	97.93
	Cell	0.001	1.533	98.56

Figure 4. (Left) Training curves of the score-matching process. The entire process of HOG-Diff is divided into two stages, *i.e.*, $K = 2$, referred to as coarse and fine, respectively. The combined loss of these two stages is labelled as Coarse+Fine. (Right) Sampling results of various topological guides.

5. Related Works

We review graph generation methods along with higher-order generation. App. C presents a more detailed review.

Deep Generative Models. Graph generative models make great progress by exploiting the capacity of deep neural networks. These models typically generate nodes and edges either in an autoregressive manner or simultaneously, utilizing techniques such as variational autoencoders (VAE) (Jin et al., 2018; Simonovsky & Komodakis, 2018), recurrent neural networks (RNN) (You et al., 2018), normalizing flows (Zang & Wang, 2020; Shi et al., 2020; Luo et al., 2021), and generative adversarial networks (GAN) (De Cao & Kipf, 2018; Martinkus et al., 2022).

Diffusion-based Graph Generation. A breakthrough in graph generative models has been marked by the recent progress in diffusion-based generative models (Niu et al., 2020). Recent models employ various strategies to enhance the generation of complex graphs, including capturing node-edge dependency (Jo et al., 2022), addressing discretization challenges (Vignac et al., 2023; Huang et al., 2023), exploiting low-to-high frequency generation curriculum (Mo et al., 2024), and improving computational efficiency through low-rank diffusion processes (Luo et al., 2023a). Recent studies have also enhanced diffusion-based generative models by incorporating diffusion bridge processes, *i.e.*, processes conditioned on the endpoints (Wu et al., 2022; Boget et al., 2024; Jo et al., 2024). Despite these advances, existing meth-

ods either overlook or inadvertently disrupt higher-order structures during graph generation, or struggle to model the topological properties, as denoising the noisy samples does not explicitly preserve the intricate structural dependencies required for generating realistic graphs.

Higher-order Generative Models. Generative modelling uses higher-order information mostly in the form of hypergraphs. Models such as Hygene (Gailhard et al., 2024) and HypeBoy (Kim et al., 2024) aim to generate hypergraphs. Dymond (Zeno et al., 2021) focuses on higher-order motifs in dynamic graphs. To the best of our knowledge, we are the first to consider higher-order guides for graph generation.

6. Conclusion

We introduce HOG-Diff, a coarse-to-fine generation framework that explicitly exploits higher-order graph topology. It decomposes the complicated generation process into easier-to-learn sub-steps, which are implemented using a generalized OU bridge process. Our theoretical analysis justifies the effectiveness of HOG-Diff over classical diffusion approaches, which is validated by superior experimental results on both molecular and generic graph generation tasks. Our framework further promises to improve interpretability by enabling the analysis of different topological guides’ performance in the generation process. This work is a key step in topological diffusion models, highlighting the impact of higher-order features absent in data and opening ample room for future work.

Impact Statement

This paper presents work whose goal is to advance the field of deep generative models. Positive applications include generating graph-structured data for scientific discovery and accelerating drug discovery by generating novel molecular structures. However, like other generative technologies, our work could potentially be misused to synthesize harmful molecules, counterfeit social interactions, or deceptive network structures.

References

- Ahmad, R. Introduction to stochastic differential equations. *Journal of the Royal Statistical Society Series C*, 37(3): 446–446, 1988.
- Anderson, B. D. Reverse-time diffusion equation models. *Stochastic Processes and their Applications*, 12(3):313–326, 1982.
- Barabási, A.-L. and Albert, R. Emergence of scaling in random networks. *Science*, 286(5439):509–512, 1999.
- Battiston, F., Cencetti, G., Iacopini, I., Latora, V., Lucas, M., Patania, A., Young, J.-G., and Petri, G. Networks beyond pairwise interactions: Structure and dynamics. *Physics Reports*, 874:1–92, 2020. ISSN 0370-1573.
- Bodnar, C., Frasca, F., Otter, N., Wang, Y., Lio, P., Montufar, G. F., and Bronstein, M. Weisfeiler and leman go cellular: Cw networks. In *Proceedings of Advances in Neural Information Processing Systems (NeurIPS)*, pp. 2625–2640, 2021.
- Boget, Y., Lavda, F., Kalousis, A., et al. Glad: Improving latent graph generative modeling with simple quantization. In *ICML 2024 Workshop on Structured Probabilistic Inference & Generative Modeling*, 2024.
- Bron, C. and Kerbosch, J. Algorithm 457: Finding all cliques of an undirected graph. *Communications of the ACM*, 16(9):575–577, sep 1973.
- Chiba, N. and Nishizeki, T. Arboricity and subgraph listing algorithms. *SIAM Journal on computing*, 14(1):210–223, 1985.
- Chung, F. R. *Spectral graph theory*, volume 92. American Mathematical Soc., 1997.
- Chung, H., Sim, B., and Ye, J. C. Come-closer-diffuse-faster: Accelerating conditional diffusion models for inverse problems through stochastic contraction. In *Proceedings of the IEEE/CVF Conference on Computer Vision and Pattern Recognition (CVPR)*, pp. 12413–12422, 2022.
- Costa, F. and Grave, K. D. Fast neighborhood subgraph pairwise distance kernel. In *Proceedings of the 27th International Conference on International Conference on Machine Learning*, pp. 255–262, 2010.
- De Cao, N. and Kipf, T. Molgan: An implicit generative model for small molecular graphs. In *ICML 2018 workshop on Theoretical Foundations and Applications of Deep Generative Models*, 2018.
- Doob, J. L. and Doob, J. *Classical potential theory and its probabilistic counterpart*, volume 262. Springer, 1984.
- Dwivedi, V. P. and Bresson, X. A generalization of transformer networks to graphs. In *AAAI Workshop on Deep Learning on Graphs: Methods and Applications*, 2021.
- Erdős, P., Rényi, A., et al. On the evolution of random graphs. *Publ. Math. Inst. Hung. Acad. Sci*, 5(1):17–60, 1960.
- Gailhard, D., Tartaglione, E., Naviner, L., and Giraldo, J. H. Hygene: A diffusion-based hypergraph generation method. *arXiv preprint arXiv:2408.16457*, 2024.
- Ghavasieh, A. and De Domenico, M. Diversity of information pathways drives sparsity in real-world networks. *Nature Physics*, 20(3):512–519, 2024.
- Hajij, M., Zamzmi, G., Papamarkou, T., Miolane, N., Guzmán-Sáenz, A., Ramamurthy, K. N., Birdal, T., Dey, T. K., Mukherjee, S., Samaga, S. N., et al. Topological deep learning: Going beyond graph data. *arXiv preprint arXiv:2206.00606*, 2022.
- Hajij, M., Zamzmi, G., Papamarkou, T., Guzman-Saenz, A., Birdal, T., and Schaub, M. T. Combinatorial complexes: bridging the gap between cell complexes and hypergraphs. In *Asilomar Conference on Signals, Systems, and Computers*, pp. 799–803. IEEE, 2023.
- Hatcher, A. *Algebraic topology*. Cambridge University Press, 2001.
- Heng, J., De Bortoli, V., Doucet, A., and Thornton, J. Simulating diffusion bridges with score matching. *arXiv preprint arXiv:2111.07243*, 2021.
- Ho, J., Jain, A., and Abbeel, P. Denoising diffusion probabilistic models. In *Proceedings of Advances in Neural Information Processing Systems (NeurIPS)*, volume 33, pp. 6840–6851, 2020.
- Huang, H., Sun, L., Du, B., and Lv, W. Conditional diffusion based on discrete graph structures for molecular graph generation. In *Proceedings of the AAAI Conference on Artificial Intelligence (AAAI)*, volume 37, pp. 4302–4311, 2023.

- Huang, Y., Zeng, Y., Wu, Q., and Lü, L. Higher-order graph convolutional network with flower-petals laplacians on simplicial complexes. In *Proceedings of the AAAI Conference on Artificial Intelligence (AAAI)*, pp. 12653–12661, 2024.
- Irwin, J. J., Sterling, T., Mysinger, M. M., Bolstad, E. S., and Coleman, R. G. Zinc: a free tool to discover chemistry for biology. *Journal of chemical information and modeling*, 52(7):1757–1768, 2012.
- Jin, W., Barzilay, R., and Jaakkola, T. Junction tree variational autoencoder for molecular graph generation. In *International Conference on Machine Learning (ICML)*, pp. 2323–2332. PMLR, 2018.
- Jo, J., Lee, S., and Hwang, S. J. Score-based generative modeling of graphs via the system of stochastic differential equations. In *International Conference on Machine Learning (ICML)*, pp. 10362–10383. PMLR, 2022.
- Jo, J., Kim, D., and Hwang, S. J. Graph generation with diffusion mixture. In *International Conference on Machine Learning (ICML)*, 2024.
- Kim, S., Kang, S., Bu, F., Lee, S. Y., Yoo, J., and Shin, K. Hypeboy: Generative self-supervised representation learning on hypergraphs. In *Proceedings of International Conference on Learning Representations (ICLR)*, 2024.
- Kipf, T. N. and Welling, M. Semi-supervised classification with graph convolutional networks. In *Proceedings of International Conference on Learning Representations (ICLR)*, 2017.
- Kusner, M. J., Paige, B., and Hernández-Lobato, J. M. Grammar variational autoencoder. In *International Conference on Machine Learning (ICML)*, volume 70 of *Proceedings of Machine Learning Research*, pp. 1945–1954, 2017.
- Landrum, G. et al. Rdkit: Open-source cheminformatics software, 2016. URL <http://www.rdkit.org/>, <https://github.com/rdkit/rdkit>, 2016.
- Li, Y., Vinyals, O., Dyer, C., Pascanu, R., and Battaglia, P. Learning deep generative models of graphs. *arXiv preprint arXiv:1803.03324*, 2018.
- Liu, C., Zhu, L., and Belkin, M. Toward a theory of optimization for over-parameterized systems of non-linear equations: the lessons of deep learning. *arXiv preprint arXiv:2003.00307*, 7, 2020.
- Liu, J., Kumar, A., Ba, J., Kiros, J., and Swersky, K. Graph normalizing flows. In *Proceedings of Advances in Neural Information Processing Systems (NeurIPS)*, volume 32, 2019.
- Liu, M., Yan, K., Oztekin, B., and Ji, S. Graphebm: Molecular graph generation with energy-based models. In *Energy Based Models Workshop-ICLR*, 2021.
- Luo, T., Mo, Z., and Pan, S. J. Fast graph generation via spectral diffusion. *IEEE Transactions on Pattern Analysis and Machine Intelligence (TPAMI)*, 2023a.
- Luo, Y., Yan, K., and Ji, S. Graphdf: A discrete flow model for molecular graph generation. In *International Conference on Machine Learning (ICML)*, pp. 7192–7203. PMLR, 2021.
- Luo, Z., Gustafsson, F. K., Zhao, Z., Sjölund, J., and Schön, T. B. Image restoration with mean-reverting stochastic differential equations. In *International Conference on Machine Learning (ICML)*, pp. 23045–23066, 2023b.
- Martinkus, K., Loukas, A., Perraudin, N., and Wattenhofer, R. Spectre: Spectral conditioning helps to overcome the expressivity limits of one-shot graph generators. In *International Conference on Machine Learning (ICML)*, pp. 15159–15179. PMLR, 2022.
- Mo, Z., Luo, T., and Pan, S. J. Graph principal flow network for conditional graph generation. In *Proceedings of the ACM on Web Conference 2024*, pp. 768–779, 2024.
- Niu, C., Song, Y., Song, J., Zhao, S., Grover, A., and Ermon, S. Permutation invariant graph generation via score-based generative modeling. In *International Conference on Artificial Intelligence and Statistics*, pp. 4474–4484. PMLR, 2020.
- Papamarkou, T., Birdal, T., Bronstein, M. M., Carlsson, G. E., Curry, J., Gao, Y., Hajj, M., Kwitt, R., Lio, P., Di Lorenzo, P., Maroulas, V., Miolane, N., Nasrin, F., Natesan Ramamurthy, K., Rieck, B., Scardapane, S., Schaub, M. T., Veličković, P., Wang, B., Wang, Y., Wei, G., and Zamzmi, G. Position: Topological deep learning is the new frontier for relational learning. In *International Conference on Machine Learning (ICML)*, volume 235, pp. 39529–39555, 2024.
- Perez, E., Strub, F., De Vries, H., Dumoulin, V., and Courville, A. Film: Visual reasoning with a general conditioning layer. In *Proceedings of the AAAI Conference on Artificial Intelligence (AAAI)*, volume 32, 2018.
- Preuer, K., Renz, P., Unterthiner, T., Hochreiter, S., and Klambauer, G. Fréchet chemnet distance: a metric for generative models for molecules in drug discovery. *Journal of chemical information and modeling*, 58(9):1736–1741, 2018.
- Ramakrishnan, R., Dral, P. O., Rupp, M., and Von Lilienfeld, O. A. Quantum chemistry structures and properties of 134 kilo molecules. *Scientific data*, 1(1):1–7, 2014.

- Salminen, P. On conditional ornstein–uhlenbeck processes. *Advances in applied probability*, 16(4):920–922, 1984.
- Shi, C., Xu, M., Zhu, Z., Zhang, W., Zhang, M., and Tang, J. Graphaf: a flow-based autoregressive model for molecular graph generation. In *Proceedings of International Conference on Learning Representations (ICLR)*, 2020.
- Simonovsky, M. and Komodakis, N. Graphvae: Towards generation of small graphs using variational autoencoders. In *International Conference on Artificial Neural Networks*, pp. 412–422, 2018.
- Song, Y. and Ermon, S. Generative modeling by estimating gradients of the data distribution. In *Proceedings of Advances in Neural Information Processing Systems (NeurIPS)*, volume 32, 2019.
- Song, Y., Sohl-Dickstein, J., Kingma, D. P., Kumar, A., Ermon, S., and Poole, B. Score-based generative modeling through stochastic differential equations. In *Proceedings of International Conference on Learning Representations (ICLR)*, 2021.
- Soviany, P., Ionescu, R. T., Rota, P., and Sebe, N. Curriculum learning: A survey. *International Journal of Computer Vision*, 130(6):1526–1565, 2022.
- Vignac, C., Krawczuk, I., Siraudin, A., Wang, B., Cevher, V., and Frossard, P. Digress: Discrete denoising diffusion for graph generation. In *Proceedings of International Conference on Learning Representations (ICLR)*, 2023.
- Vincent, P. A connection between score matching and denoising autoencoders. *Neural computation*, 23(7):1661–1674, 2011.
- Waswani, A., Shazeer, N., Parmar, N., Uszkoreit, J., Jones, L., Gomez, A., Kaiser, L., and Polosukhin, I. Attention is all you need. In *Proceedings of Advances in Neural Information Processing Systems (NeurIPS)*, 2017.
- Wu, L., Gong, C., Liu, X., Ye, M., and Liu, Q. Diffusion-based molecule generation with informative prior bridges. *Proceedings of Advances in Neural Information Processing Systems (NeurIPS)*, 35:36533–36545, 2022.
- Xiao, Z. and Blanco, E. Are people located in the places they mention in their tweets? a multimodal approach. In *International Conference on Computational Linguistics*, pp. 2561–2571, 2022.
- You, J., Ying, R., Ren, X., Hamilton, W., and Leskovec, J. Graphrnn: Generating realistic graphs with deep autoregressive models. In *International Conference on Machine Learning (ICML)*, pp. 5708–5717. PMLR, 2018.
- Yue, C., Peng, Z., Ma, J., Du, S., Wei, P., and Zhang, D. Image restoration through generalized ornstein-uhlenbeck bridge. In *International Conference on Machine Learning (ICML)*, 2024.
- Zang, C. and Wang, F. Moflow: an invertible flow model for generating molecular graphs. In *Proceedings of the 26th ACM SIGKDD international conference on knowledge discovery & data mining*, pp. 617–626, 2020.
- Zeng, Y., Huang, Y., Ren, X.-L., and Lü, L. Identifying vital nodes through augmented random walks on higher-order networks. *Information Sciences*, pp. 121067, 2024a.
- Zeng, Y., Huang, Y., Wu, Q., and Lü, L. Influential simplices mining via simplicial convolutional networks. *Information Processing & Management*, 61(5):103813, 2024b.
- Zeno, G., La Fond, T., and Neville, J. Dymond: Dynamic motif-nodes network generative model. In *Proceedings of the Web Conference 2021*, pp. 718–729, 2021.
- Zhu, Y., Du, Y., Wang, Y., Xu, Y., Zhang, J., Liu, Q., and Wu, S. A survey on deep graph generation: Methods and applications. In *Learning on Graphs Conference*, pp. 47–1. PMLR, 2022.

Appendix

Organization. The appendix is structured as follows: We first present the derivations excluded from the main paper due to space limitation in Section A. Section B introduces the concept and examples of higher-order networks. Additional explanations on related work are provided in Section C. Section D details the generation process, including the architecture of the proposed denoising network, as well as the training and sampling procedures. Computational efficiency is discussed in Section E. Section F outlines the experimental setup, and Section G concludes with visualizations of the generated samples.

A. Formal Statements and Proofs

This section presents the formal statements of key theoretical results and their detailed derivations. We will recall and more precisely state the propositions before presenting the proof.

A.1. Diffusion Bridge Process

In the following, we derive the Generalized Ornstein-Uhlenbeck (GOU) bridge process using Doob's h -transform (Doob & Doob, 1984) and analyze its relationship with the Brownian bridge process.

Recall that the generalized Ornstein-Uhlenbeck (GOU) process is the time-varying OU process. It is a stationary Gaussian-Markov process whose marginal distribution gradually tends towards a stable mean and variance over time. The GOU process \mathbb{Q} is generally defined as follows (Ahmad, 1988; Luo et al., 2023b):

$$\mathbb{Q} : d\mathbf{G}_t = \theta_t (\boldsymbol{\mu} - \mathbf{G}_t) dt + g_t d\mathbf{W}_t, \quad (13)$$

where $\boldsymbol{\mu}$ is a given state vector, θ_t denotes a scalar drift coefficient and g_t represents the diffusion coefficient. At the same time, we require θ_t, g_t to satisfy the specified relationship $2\sigma^2 = g_t^2/\theta_t$, where σ^2 is a given constant scalar. As a result, its transition probability possesses a closed-form analytical solution:

$$\begin{aligned} p(\mathbf{G}_t | \mathbf{G}_s) &= \mathcal{N}(\mathbf{m}_{s:t}, v_{s:t}^2 \mathbf{I}), \\ \mathbf{m}_{s:t} &= \boldsymbol{\mu} + (\mathbf{G}_s - \boldsymbol{\mu}) e^{-\bar{\theta}_{s:t}}, \\ v_{s:t}^2 &= \sigma^2 \left(1 - e^{-2\bar{\theta}_{s:t}}\right). \end{aligned} \quad (14)$$

Here, $\bar{\theta}_{s:t} = \int_s^t \theta_z dz$. When the starting time $t = 0$, we substitute $\bar{\theta}_{0:t}$ with $\bar{\theta}_t$ for notation simplicity.

Proposition 3.2. Let \mathbf{G}_t evolve according to the generalized OU process in Eq. (8), subject to the terminal conditional $\boldsymbol{\mu} = \mathbf{G}_{\tau_k}$. The conditional marginal distribution $p(\mathbf{G}_t | \mathbf{G}_{\tau_k})$ then evolves according to the following SDE:

$$d\mathbf{G}_t = \theta_t \left(1 + \frac{2}{e^{2\bar{\theta}_{t:\tau_k}} - 1}\right) (\mathbf{G}_{\tau_k} - \mathbf{G}_t) dt + g_{k,t} d\mathbf{W}_t. \quad (15)$$

The conditional transition probability $p(\mathbf{G}_t | \mathbf{G}_{\tau_{k-1}}, \mathbf{G}_{\tau_k})$ has analytical form as follows:

$$\begin{aligned} p(\mathbf{G}_t | \mathbf{G}_{\tau_{k-1}}, \mathbf{G}_{\tau_k}) &= \mathcal{N}(\bar{\mathbf{m}}_t, \bar{v}_t^2 \mathbf{I}), \\ \bar{\mathbf{m}}_t &= \mathbf{G}_{\tau_k} + (\mathbf{G}_{\tau_{k-1}} - \mathbf{G}_{\tau_k}) e^{-\bar{\theta}_{\tau_{k-1}:t}} \frac{v_{t:\tau_k}^2}{v_{\tau_{k-1}:\tau_k}^2}, \\ \bar{v}_t^2 &= v_{\tau_{k-1}:t}^2 v_{t:\tau_k}^2 / v_{\tau_{k-1}:\tau_k}^2. \end{aligned} \quad (16)$$

Here, $\bar{\theta}_{a:b} = \int_a^b \theta_s ds$, and $v_{a:b} = \sigma^2(1 - e^{-2\bar{\theta}_{a:b}})$.

Proof. To simplify the notion, in the k -th generation step, we adopt the following conventions: $T = \tau_k$, $\mathbf{x}_t = \mathbf{G}_t^{(k)}$, $0 = \tau_{k-1}$, $\mathbf{x}_0 = \mathbf{G}_{\tau_{k-1}}$, $\mathbf{x}_T = \mathbf{G}_{\tau_k}$.

From Eq. (9), we can derive the following conditional distribution

$$p(\mathbf{x}_T | \mathbf{x}_t) = \mathcal{N}(\mathbf{x}_T + (\mathbf{x}_t - \mathbf{x}_T) e^{\bar{\theta}_{t:T}}, v_{t:T}^2 \mathbf{I}). \quad (17)$$

Hence, the h -function can be directly computed as:

$$\begin{aligned}
 \mathbf{h}(\mathbf{x}_t, t, \mathbf{x}_T, T) &= \nabla_{\mathbf{x}_t} \log p(\mathbf{x}_T | \mathbf{x}_t) \\
 &= -\nabla_{\mathbf{x}_t} \left[\frac{(\mathbf{x}_t - \mathbf{x}_T)^2 e^{-2\bar{\theta}_{t:T}}}{2v_{t:T}^2} + const \right] \\
 &= (\mathbf{x}_T - \mathbf{x}_t) \frac{e^{-2\bar{\theta}_{t:T}}}{v_{t:T}^2} \\
 &= (\mathbf{x}_T - \mathbf{x}_t) \sigma^{-2} / (e^{2\bar{\theta}_{t:T}} - 1).
 \end{aligned} \tag{18}$$

Then the Doob's h -transform yields the representation of an endpoint \mathbf{x}_T conditioned process defined by the following SDE:

$$\begin{aligned}
 d\mathbf{x}_t &= [f(\mathbf{x}_t, t) + g_t^2 \mathbf{h}(\mathbf{x}_t, t, \mathbf{x}_T, T)] dt + g_t d\mathbf{w}_t \\
 &= \left(\theta_t + \frac{g_t^2}{\sigma^2 (e^{2\bar{\theta}_{t:T}} - 1)} \right) (\mathbf{x}_T - \mathbf{x}_t) dt + g_t d\mathbf{w}_t \\
 &= \theta_t \left(1 + \frac{2}{e^{2\bar{\theta}_{t:T}} - 1} \right) (\mathbf{x}_T - \mathbf{x}_t) dt + g_t d\mathbf{w}_t.
 \end{aligned} \tag{19}$$

Given that the joint distribution of $[\mathbf{x}_0, \mathbf{x}_t, \mathbf{x}_T]$ is multivariate normal, the conditional distribution $p(\mathbf{x}_t | \mathbf{x}_0, \mathbf{x}_T)$ is also Gaussian:

$$p(\mathbf{x}_t | \mathbf{x}_0, \mathbf{x}_T) = \mathcal{N}(\bar{\mathbf{m}}_t, \bar{v}_t^2 \mathbf{I}), \tag{20}$$

where the mean $\bar{\mathbf{m}}_t$ and variance \bar{v}_t^2 are determined using the conditional formulas for multivariate normal variables:

$$\begin{aligned}
 \bar{\mathbf{m}}_t &= \mathbb{E}[\mathbf{x}_t | \mathbf{x}_0, \mathbf{x}_T] = \mathbb{E}[\mathbf{x}_t | \mathbf{x}_0] + \text{Cov}(\mathbf{x}_t, \mathbf{x}_T | \mathbf{x}_0) \text{Var}(\mathbf{x}_T | \mathbf{x}_0)^{-1} (\mathbf{x}_T - \mathbb{E}[\mathbf{x}_T | \mathbf{x}_0]), \\
 \bar{v}_t^2 &= \text{Var}(\mathbf{x}_t | \mathbf{x}_0, \mathbf{x}_T) = \text{Var}(\mathbf{x}_t | \mathbf{x}_0) - \text{Cov}(\mathbf{x}_t, \mathbf{x}_T | \mathbf{x}_0) \text{Var}(\mathbf{x}_T | \mathbf{x}_0)^{-1} \text{Cov}(\mathbf{x}_T, \mathbf{x}_t | \mathbf{x}_0).
 \end{aligned} \tag{21}$$

Notice that

$$\text{Cov}(\mathbf{x}_t, \mathbf{x}_T | \mathbf{x}_0) = \text{Cov}(\mathbf{x}_t, (\mathbf{x}_t - \mathbf{x}_T) e^{-\bar{\theta}_{t:T}} | \mathbf{x}_0) = e^{-\bar{\theta}_{t:T}} \text{Var}(\mathbf{x}_t | \mathbf{x}_0). \tag{22}$$

By substituting this and the results in Eq. (9) into Eq. (21), we can obtain

$$\begin{aligned}
 \bar{\mathbf{m}}_t &= \left(\mathbf{x}_T + (\mathbf{x}_0 - \mathbf{x}_T) e^{-\bar{\theta}_t} \right) + \left(e^{-\bar{\theta}_{t:T}} v_t^2 \right) / v_T^2 \cdot \left(\mathbf{x}_T - \mathbf{x}_T - (\mathbf{x}_0 - \mathbf{x}_T) e^{-\bar{\theta}_T} \right) \\
 &= \mathbf{x}_T + (\mathbf{x}_0 - \mathbf{x}_T) \left(e^{-\bar{\theta}_t} - e^{-\bar{\theta}_{t:T}} e^{-\bar{\theta}_T} v_t^2 / v_T^2 \right) \\
 &= \mathbf{x}_T + (\mathbf{x}_0 - \mathbf{x}_T) e^{-\bar{\theta}_t} \left(\frac{1 - e^{-2\bar{\theta}_T} - e^{-2\bar{\theta}_{t:T}} (1 - e^{-2\bar{\theta}_t})}{1 - e^{-2\bar{\theta}_T}} \right) \\
 &= \mathbf{x}_T + (\mathbf{x}_0 - \mathbf{x}_T) e^{-\bar{\theta}_t} v_{t:T}^2 / v_T^2,
 \end{aligned} \tag{23}$$

and

$$\begin{aligned}
 \bar{v}_t^2 &= v_t^2 - \left(e^{-\bar{\theta}_{t:T}} v_t^2 \right)^2 / v_T^2 \\
 &= \frac{v_t^2}{v_T^2} (v_T^2 - e^{-2\bar{\theta}_{t:T}} v_t^2) \\
 &= \frac{v_t^2}{v_T^2} \sigma^2 \left(1 - e^{-2\bar{\theta}_T} - e^{-2\bar{\theta}_{t:T}} (1 - e^{-2\bar{\theta}_t}) \right) \\
 &= v_t^2 v_{t:T}^2 / v_T^2.
 \end{aligned} \tag{24}$$

Finally, we conclude the proof by reverting to the original notations. \square

Note that the generalized OU bridge process, also referred to as the conditional GOU process, has been studied theoretically in previous works (Salminen, 1984; Heng et al., 2021; Yue et al., 2024). However, we are the first to demonstrate its effectiveness in explicitly learning higher-order structures within the graph generation process.

Brownian Bridge Process. In the following, we demonstrate that the Brownian bridge process is a particular case of the generalized OU bridge process when θ_t approaches zero.

Assume $\theta_t = \theta$ is a constant that tends to zero, we obtain

$$\bar{\theta}_{a:b} = \int_a^b \theta_s ds = \theta(b-a) \rightarrow 0. \quad (25)$$

Consider the term $e^{2\bar{\theta}_{t:\tau_k}} - 1$, we approximate the exponential function using a first-order Taylor expansion for small $\bar{\theta}_{t:\tau_k}$:

$$e^{2\bar{\theta}_{t:\tau_k}} - 1 \approx 2\bar{\theta}_{t:\tau_k} \rightarrow 2\theta(\tau_k - t). \quad (26)$$

Hence, the drift term in the generalized OU bridge simplifies to

$$\theta_t \left(1 + \frac{2}{e^{2\bar{\theta}_{t:\tau_k}} - 1} \right) \approx \theta \left(1 + \frac{2}{2\theta(\tau_k - t)} \right) \rightarrow \frac{1}{\tau_k - t}. \quad (27)$$

Consequently, in the limit $\theta_t \rightarrow 0$, the generalized OU bridge process described in Eq. (15) can be modelled by the following SDE:

$$d\mathbf{G}_t = \frac{\mathbf{G}_{\tau_k} - \mathbf{G}_t}{\tau_k - t} dt + g_{k,t} d\mathbf{W}_t. \quad (28)$$

This equation precisely corresponds to the SDE representation of the classical Brownian bridge process.

In contrast to the generalized OU bridge process in Eq. (15), the evolution of the Brownian bridge is fully determined by the noise schedule $g_{k,t}$, resulting in a simpler SDE representation. However, this constraint in the Brownian bridge reduces the flexibility in designing the generative process.

Note that the Brownian bridge is an endpoint-conditioned process relative to a reference Brownian motion, which the SDE governs:

$$d\mathbf{G}_t = g_t d\mathbf{W}_t. \quad (29)$$

This equation describes a pure diffusion process without drift, making it a specific instance of the generalized OU process in Eq. (8).

A.2. Proof of Proposition 3.3

To establish proof, we begin by introducing essential definitions and assumptions.

Definition A.1 (β -smooth). A function $f : \mathbb{R}^m \rightarrow \mathbb{R}^n$ is said to be β -smooth if and only if

$$\|f(\mathbf{w}) - f(\mathbf{v}) - \nabla f(\mathbf{v})(\mathbf{w} - \mathbf{v})\| \leq \frac{\beta}{2} \|\mathbf{w} - \mathbf{v}\|^2, \forall \mathbf{w}, \mathbf{v} \in \mathbb{R}^m. \quad (30)$$

Proposition 3.3 (Formal). *Let $\ell^{(k)}(\boldsymbol{\theta})$ be a loss function that is β -smooth and satisfies the μ -PL (Polyak-Łojasiewicz) condition in the ball $B(\boldsymbol{\theta}_0, R)$ of radius $R = 2N\sqrt{2\beta\ell^{(k)}(\boldsymbol{\theta}_0)}/(\mu\delta)$, where $\delta > 0$. Then, with probability $1 - \delta$ over the choice of mini-batch of size b , stochastic gradient descent (SGD) with a learning rate $\eta^* = \frac{\mu N}{N\beta(N^2\beta + \mu(b-1))}$ converges to a global solution in the ball B with exponential convergence rate:*

$$\mathbb{E} \left[\ell^{(k)}(\boldsymbol{\theta}_i) \right] \leq \left(1 - \frac{b\mu^2}{\beta N(\beta N^2 + \mu(b-1))} \right)^i \ell^{(k)}(\boldsymbol{\theta}_0). \quad (31)$$

Here, N denotes the size of the training dataset. Furthermore, the proposed generative model yields a smaller smoothness constant $\beta_{\text{HOG-Diff}}$ compared to that of the classical model $\beta_{\text{classical}}$, i.e., $\beta_{\text{HOG-Diff}} \leq \beta_{\text{classical}}$, implying that the learned distribution in HOG-Diff converges to the target distribution faster than classical generative models.

Proof. Assume that the loss function $\ell^{(k)}(\boldsymbol{\theta})$ in Eq. (11) is minimized using standard Stochastic Gradient Descent (SGD) on a training dataset $\mathcal{S} = \{\mathbf{x}^i\}_{i=1}^N$. At the i -th iteration, parameter $\boldsymbol{\theta}_i$ is updated using a mini-batch of size b as follows:

$$\boldsymbol{\theta}_{i+1} \triangleq \boldsymbol{\theta}_i - \eta \nabla \ell^{(k)}(\boldsymbol{\theta}_i), \quad (32)$$

where η is the learning rate.

Following Liu et al. (2020) and Luo et al. (2023a), we assume that $\ell^{(k)}(\boldsymbol{\theta})$ is β -smooth and satisfies the μ -PL condition in the ball $B(\boldsymbol{\theta}_0, R)$ with $R = 2N\sqrt{2\beta\ell^{(k)}(\boldsymbol{\theta}_0)}/(\mu\delta)$ where $\delta > 0$. Then, with probability $1 - \delta$ over the choice of mini-batch of size b , SGD with a learning rate $\eta^* = \frac{\mu N}{N\beta(N^2\beta + \mu(b-1))}$ converges to a global solution in the ball $B(\boldsymbol{\theta}_0, R)$ with exponential convergence rate (Liu et al., 2020):

$$\mathbb{E}[\ell^{(k)}(\boldsymbol{\theta}_i)] \leq \left(1 - \frac{b\mu\eta^*}{N}\right)^i \ell^{(k)}(\boldsymbol{\theta}_0) = \left(1 - \frac{b\mu^2}{\beta N(\beta N^2 + \mu(b-1))}\right)^i \ell^{(k)}(\boldsymbol{\theta}_0). \quad (33)$$

Next, we show that the proposed framework has a smaller smoothness constant than the classical one-step model. Therefore, we focus exclusively on the spectral component $\|\mathbf{s}_{\boldsymbol{\theta}, \Lambda}^{(k)} - \nabla_{\Lambda} \log p_t(\mathbf{G}_t | \mathbf{G}_{\tau_k})\|_2^2$ from the full loss function in Eq. (11), as the feature-related part of the loss function in HOG-Diff aligns with that of the classical framework. For simplicity, we use the notation $\bar{\ell}(\boldsymbol{\theta}) = \|\mathbf{s}_{\boldsymbol{\theta}, \Lambda}^{(k)} - \nabla_{\Lambda} \log p_t(\mathbf{G}_t | \mathbf{G}_{\tau_k})\|^2 = \|\mathbf{s}_{\boldsymbol{\theta}}(\mathbf{x}_t) - \nabla_{\mathbf{x}} \log p_t(\mathbf{x}_t)\|^2$ as the feature-related part of the loss.

Next, we verify that $\bar{\ell}(\boldsymbol{\theta})$ is β -smooth under the assumptions given. Notice that the gradient of the loss function is given by:

$$\nabla \bar{\ell}(\boldsymbol{\theta}) = 2\mathbb{E}[(\mathbf{s}_{\boldsymbol{\theta}}(\mathbf{x}) - \nabla \log p(\mathbf{x}))^{\top} \nabla_{\boldsymbol{\theta}} \mathbf{s}_{\boldsymbol{\theta}}(\mathbf{x})] \quad (34)$$

Hence,

$$\begin{aligned} \|\nabla \bar{\ell}(\boldsymbol{\theta}_1) - \nabla \bar{\ell}(\boldsymbol{\theta}_2)\| &= 2\|\mathbb{E}[(\mathbf{s}_{\boldsymbol{\theta}_1}(\mathbf{x}) - \nabla \log p(\mathbf{x}))^{\top} \nabla_{\boldsymbol{\theta}_1} \mathbf{s}_{\boldsymbol{\theta}_1}(\mathbf{x}) - (\mathbf{s}_{\boldsymbol{\theta}_2}(\mathbf{x}) - \nabla \log p(\mathbf{x}))^{\top} \nabla_{\boldsymbol{\theta}_2} \mathbf{s}_{\boldsymbol{\theta}_2}(\mathbf{x})]\| \\ &\leq 2\mathbb{E}[\|\mathbf{s}_{\boldsymbol{\theta}_1}(\mathbf{x}) - \mathbf{s}_{\boldsymbol{\theta}_2}(\mathbf{x})\| \cdot \|\nabla_{\boldsymbol{\theta}_1} \mathbf{s}_{\boldsymbol{\theta}_1}(\mathbf{x})\| + \|\mathbf{s}_{\boldsymbol{\theta}_2}(\mathbf{x}) - \nabla \log p(\mathbf{x})\| \cdot \|\nabla_{\boldsymbol{\theta}_1} \mathbf{s}_{\boldsymbol{\theta}_1}(\mathbf{x}) - \nabla_{\boldsymbol{\theta}_2} \mathbf{s}_{\boldsymbol{\theta}_2}(\mathbf{x})\|]. \end{aligned} \quad (35)$$

Suppose $\|\nabla_{\boldsymbol{\theta}} \mathbf{s}_{\boldsymbol{\theta}}(\mathbf{x})\| \leq C_1$ and $\|\mathbf{s}_{\boldsymbol{\theta}}(\mathbf{x}) - \nabla \log p(\mathbf{x})\| \leq C_2$, then we can obtain

$$\begin{aligned} \|\nabla \bar{\ell}(\boldsymbol{\theta}_1) - \nabla \bar{\ell}(\boldsymbol{\theta}_2)\| &\leq 2\mathbb{E}[C_1\beta_{\mathbf{s}_{\boldsymbol{\theta}}}\|\boldsymbol{\theta}_1 - \boldsymbol{\theta}_2\| + C_2\beta_{\nabla_{\boldsymbol{\theta}}\mathbf{s}_{\boldsymbol{\theta}}}\|\boldsymbol{\theta}_1 - \boldsymbol{\theta}_2\|] \\ &= 2(\beta_{\mathbf{s}_{\boldsymbol{\theta}}}C_1 + C_2\beta_{\nabla_{\boldsymbol{\theta}}\mathbf{s}_{\boldsymbol{\theta}}})\|\boldsymbol{\theta}_1 - \boldsymbol{\theta}_2\|. \end{aligned} \quad (36)$$

To satisfy the β -smooth of $\bar{\ell}(\boldsymbol{\theta})$, we require that

$$2(C_1\beta_{\mathbf{s}_{\boldsymbol{\theta}}} + C_2\beta_{\nabla_{\boldsymbol{\theta}}\mathbf{s}_{\boldsymbol{\theta}}}) \leq \beta. \quad (37)$$

This implies that the distribution learned by the proposed framework can converge to the target distribution. Therefore, following Chung et al. (2022), we further assume that $\mathbf{s}_{\boldsymbol{\theta}}$ is a sufficiently expressive parameterized score function so that $\beta_{\mathbf{s}_{\boldsymbol{\theta}}} = \beta_{\nabla \log p_t | \tau_{k-1}}$ and $\beta_{\nabla^2 \mathbf{s}_{\boldsymbol{\theta}}} = \beta_{\nabla^2 \log p_t | \tau_{k-1}}$.

Consider the loss function of classical generative models goes as: $\bar{\ell}(\boldsymbol{\varphi}) = \mathbb{E}\|\mathbf{s}_{\boldsymbol{\varphi}}(\mathbf{x}_t) - \nabla_{\mathbf{x}_t} q_t(\mathbf{x}_t | \mathbf{x}_0)\|^2$. To demonstrate that the proposed framework converges faster to the target distribution compared to the classical one-step generation framework, it suffices to show that: $\beta_{\nabla p_t | \tau_{k-1}} \leq \beta_{\nabla q_t | 0}$ and $\beta_{\nabla^2 p_t | \tau_{k-1}} \leq \beta_{\nabla^2 q_t | 0}$.

Let $\mathbf{x} \sim q_t | 0$ and $\mathbf{x}' \sim p_t | \tau_{k-1}$. Since we inject topological information from \mathbf{x} into \mathbf{x}' , \mathbf{x}' can be viewed as being obtained by adding noise to \mathbf{x} . Hence, we can model \mathbf{x}' as $\mathbf{x}' = \mathbf{x} + \epsilon$ where $\epsilon \sim \mathcal{N}(\mathbf{0}, \sigma^2 \mathbf{I})$. The variance of Gaussian noise σ^2 controls the information remained in \mathbf{x}' . Hence, its distribution can be expressed as $p(\mathbf{x}') = \int q(\mathbf{x}' - \epsilon)\pi(\epsilon) d\epsilon$.

Therefore, we can obtain

$$\begin{aligned} \|\nabla_{\mathbf{x}'}^k p(\mathbf{x}'_1) - \nabla_{\mathbf{x}'}^k p(\mathbf{x}'_2)\| &= \|\nabla_{\mathbf{x}'}^k \int (q(\mathbf{x}'_1 - \epsilon) - q(\mathbf{x}'_2 - \epsilon)) \pi(\epsilon) d\epsilon\| \\ &\leq \int \|\nabla_{\mathbf{x}'}^k q(\mathbf{x}'_1 - \epsilon) - \nabla_{\mathbf{x}'}^k q(\mathbf{x}'_2 - \epsilon)\| \pi(\epsilon) d\epsilon \\ &\leq \|\nabla_{\mathbf{x}'}^k q(\mathbf{x}')\|_{\text{lip}}(\mathbf{x}'_1 - \mathbf{x}'_2) \int \pi(\epsilon) d\epsilon \\ &\leq \|\nabla_{\mathbf{x}'}^k q(\mathbf{x}')\|_{\text{lip}}(\mathbf{x}'_1 - \mathbf{x}'_2). \end{aligned} \quad (38)$$

Hence, $\|\nabla_{\mathbf{x}'}^k \log p(\mathbf{x}')\|_{\text{lip}} \leq \|\nabla_{\mathbf{x}'}^k \log q(\mathbf{x}')\|_{\text{lip}}$.

By setting $k = 3$ and $k = 4$, we can obtain $\beta_{\nabla \log p_t|\tau_{k-1}} \leq \beta_{\nabla \log q_t|0}$ and $\beta_{\nabla^2 \log p_t|\tau_{k-1}} \leq \beta_{\nabla^2 \log q_t|0}$. Therefore $\beta_{\text{HOG-Diff}} \leq \beta_{\text{classical}}$, implying that the training process of HOG-Diff (\mathbf{s}_θ) will converge faster than the classical generative framework (\mathbf{s}_φ).

□

A.3. Proof of Proposition 3.4

Here, we denote the expected reconstruction error at each generation process as $\mathcal{E}(t) = \mathbb{E} \left\| \bar{\mathbf{G}}_t - \hat{\mathbf{G}}_t \right\|^2$.

Proposition 3.4. *Under appropriate Lipschitz and boundedness assumptions, the reconstruction error of HOG-Diff satisfies the following bound:*

$$\mathcal{E}(0) \leq \alpha(0) \exp \int_0^{\tau_1} \gamma(s) ds, \quad (39)$$

where $\alpha(0) = C^2 \ell^{(1)}(\boldsymbol{\theta}) \int_0^{\tau_1} g_{1,s}^4 ds + C \mathcal{E}(\tau_1) \int_0^{\tau_1} h_{1,s}^2 ds$, $\gamma(s) = C^2 g_{1,s}^4 \|\mathbf{s}_\theta(\cdot, s)\|_{\text{lip}}^2 + C \|h_{1,s}\|_{\text{lip}}^2$, and $h_{1,s} = \theta_s \left(1 + \frac{2}{e^{2\theta_s \tau_1 - 1}}\right)$. Furthermore, we can derive that the reconstruction error bound of HOG-Diff is sharper than classical graph generation models.

Proof. Let $\mathcal{E}(t) = \mathbb{E} \left\| \bar{\mathbf{G}}_t - \hat{\mathbf{G}}_t \right\|^2$, which reflects the expected error between the data reconstructed with the ground truth score $\nabla \log p_t(\cdot)$ and the learned scores $\mathbf{s}_\theta(\cdot)$. In particular, $\bar{\mathbf{G}}$ is obtained by solving the following oracle reversed time SDE:

$$d\bar{\mathbf{G}}_t = (\mathbf{f}_{k,t}(\bar{\mathbf{G}}_t) - g_{k,t}^2 \nabla_{\mathbf{G}} \log p_t(\bar{\mathbf{G}}_t)) d\bar{t} + g_{k,t} d\bar{\mathbf{W}}_t, t \in [\tau_{k-1}, \tau_k], \quad (40)$$

whereas $\hat{\mathbf{G}}_t$ is governed based on the corresponding estimated reverse time SDE:

$$d\hat{\mathbf{G}}_t = (\mathbf{f}_{k,t}(\hat{\mathbf{G}}_t) - g_{k,t}^2 \mathbf{s}_\theta(\hat{\mathbf{G}}_t, t)) d\bar{t} + g_{k,t} d\bar{\mathbf{W}}_t, t \in [\tau_{k-1}, \tau_k]. \quad (41)$$

Here, $\mathbf{f}_{k,t}$ is the drift function of the Ornstein–Uhlenbeck bridge. For simplicity, we denote the Lipschitz norm by $\|\cdot\|_{\text{lip}}$ and $\mathbf{f}_{k,s}(\mathbf{G}_s) = h_{k,s}(\mathbf{G}_{\tau_k} - \mathbf{G}_s)$, where $h_{k,s} = \theta_s \left(1 + \frac{2}{e^{2\theta_s \tau_k - 1}}\right)$.

To bound the expected reconstruction error $\mathbb{E} \left\| \bar{\mathbf{G}}_{\tau_{k-1}} - \hat{\mathbf{G}}_{\tau_{k-1}} \right\|^2$ at each generation process, we begin by analyze how $\mathbb{E} \left\| \bar{\mathbf{G}}_t - \hat{\mathbf{G}}_t \right\|^2$ evolves as time t is reversed from τ_k to τ_{k-1} . The reconstruction error goes as follows

$$\begin{aligned} \mathcal{E}(t) &\leq \mathbb{E} \int_{\tau_k}^t \left\| (\mathbf{f}_{k,s}(\bar{\mathbf{G}}_s) - \mathbf{f}_{k,s}(\hat{\mathbf{G}}_s)) + g_{k,s}^2 (\mathbf{s}_\theta(\hat{\mathbf{G}}_s, s) - \nabla_{\mathbf{G}} \log p_s(\bar{\mathbf{G}}_s)) \right\|^2 d\bar{s} \\ &\leq C \mathbb{E} \int_{\tau_k}^t \left\| \mathbf{f}_{k,s}(\bar{\mathbf{G}}_s) - \mathbf{f}_{k,s}(\hat{\mathbf{G}}_s) \right\|^2 d\bar{s} + C \mathbb{E} \int_{\tau_k}^t g_{k,s}^4 \left\| \mathbf{s}_\theta(\hat{\mathbf{G}}_s, s) - \nabla_{\mathbf{G}} \log p_s(\bar{\mathbf{G}}_s) \right\|^2 d\bar{s} \\ &\leq C \int_{\tau_k}^t \|h_{k,s}\|_{\text{lip}}^2 \cdot \mathcal{E}(s) d\bar{s} + C \mathcal{E}(\tau_k) \int_{\tau_k}^t h_{k,s}^2 d\bar{s} \\ &\quad + C^2 \int_{\tau_k}^t g_{k,s}^4 \cdot \mathbb{E} \left\| \mathbf{s}_\theta(\hat{\mathbf{G}}_s, s) - \mathbf{s}_\theta(\bar{\mathbf{G}}_s, s) \right\|^2 + g_{k,s}^4 \cdot \mathbb{E} \left\| \mathbf{s}_\theta(\bar{\mathbf{G}}_s, s) - \nabla_{\mathbf{G}} \log p_s(\bar{\mathbf{G}}_s) \right\|^2 d\bar{s} \\ &\leq \underbrace{C^2 \ell^{(k)}(\boldsymbol{\theta}) \int_{\tau_k}^t g_{k,s}^4 d\bar{s} + C \mathcal{E}(\tau_k) \int_{\tau_k}^t h_{k,s}^2 d\bar{s}}_{\alpha(t)} + \underbrace{\int_{\tau_k}^t (C^2 g_{k,s}^4 \|\mathbf{s}_\theta(\cdot, s)\|_{\text{lip}}^2 + C \|h_{k,s}\|_{\text{lip}}^2)}_{\gamma(s)} \mathcal{E}(s) d\bar{s} \\ &= \alpha(t) + \int_{\tau_k}^t \gamma(s) \mathcal{E}(s) d\bar{s}. \end{aligned} \quad (42)$$

Let $v(t) = \mathcal{E}(\tau_k - t)$ and $s' = \tau_k - s$, it can be derived that

$$v(t) = \mathcal{E}(\tau_k - t) \leq \alpha(\tau_k - t) + \int_0^t \gamma(\tau_k - s')v(s') ds'. \quad (43)$$

Here, $\alpha(\tau_k - t)$ is a non-decreasing function. By applying Grönwall's inequality, we can derive that

$$v(t) \leq \alpha(\tau_k - t) \exp \int_0^t \gamma(\tau_k - s') ds' \quad (44)$$

$$= \alpha(\tau_k - t) \exp \int_{\tau_k - t}^{\tau_k} \gamma(s) ds. \quad (45)$$

Hence,

$$\mathcal{E}(t) \leq \alpha(t) \exp \int_t^{\tau_k} \gamma(s) ds. \quad (46)$$

Therefore, the reconstruction error of HOG-Diff is bounded by

$$\begin{aligned} \mathcal{E}(0) &\leq \alpha(0) \exp \int_0^{\tau_1} \gamma(s) ds \\ &= \left(C^2 \ell^{(1)}(\boldsymbol{\theta}) \int_0^{\tau_1} g_{1,s}^4 ds + C \mathcal{E}(\tau_1) \int_0^{\tau_1} h_{1,s}^2 ds \right) \exp \int_0^{\tau_1} \gamma(s) ds. \end{aligned} \quad (47)$$

A comparable calculation for a classical graph generation model (with diffusion interval $[0, T]$) yields a bound

$$\mathcal{E}'(0) \leq \left(C^2 \ell(\boldsymbol{\varphi}) \int_0^T g_s^4 ds + C \mathcal{E}'(T) \int_0^T h_s^2 ds \right) \exp \int_0^T \gamma'(s) ds, \quad (48)$$

where $h_s = \theta_s \left(1 + \frac{2}{e^{2\theta_s T} - 1} \right)$.

Let $h(s, \tau) = \theta_s \left(1 + \frac{2}{e^{2\theta_s \tau} - 1} \right)$, $a(\tau) = \int_0^\tau h(s, \tau)^2 ds$, and $b(\tau) = \int_0^\tau \|h(s, \tau)\|_{\text{lip}}^2 ds$. Since $\tau_1 \leq T$, it follows that $\mathcal{E}(\tau_1) \leq \mathcal{E}'(T)$. Additionally, by Prop. 3.3, $\ell(\cdot)$ converges exponentially in the score-matching process. Therefore, to prove $\mathcal{E}(0) \leq \mathcal{E}'(0)$, it suffices to show that both $a(\tau)$ and $b(\tau)$ are increasing functions.

Applying the Leibniz Integral Rule, we obtain:

$$a'(\tau) = h(\tau, \tau)^2 + \int_0^\tau \frac{\partial}{\partial \tau} h(s, \tau)^2 ds \quad \text{and} \quad b'(\tau) = \|h(\tau, \tau)\|_{\text{lip}}^2 + \int_0^\tau \frac{\partial}{\partial \tau} \|h(s, \tau)\|_{\text{lip}}^2 ds. \quad (49)$$

Since $h(\tau, \tau) \rightarrow 0$, we can derive that $a'(\tau) > 0$ and $b'(\tau) > 0$. This implies $\int_0^{\tau_1} h_{1,s}^2 ds \leq \int_0^T h_s^2 ds$ and $\int_0^{\tau_1} \gamma(s) ds \leq \int_0^T \gamma'(s) ds$. Combining these inequalities, we can finally conclude $\mathcal{E}(0) \leq \mathcal{E}'(0)$. Therefore, HOG-Diff provides a sharper reconstruction error bound than the classical graph generation framework. \square

B. Higher-order Networks

Graphs are elegant and useful abstractions for modelling irregular relationships in empirical systems, but their inherent limitation to pairwise interactions restricts their representation of group dynamics (Battiston et al., 2020; Xiao & Blanco, 2022). For example, cyclic structures like benzene rings and functional groups play a holistic role in molecular networks; densely interconnected structures, like simplices, often have a collective influence on social networks; and functional brain networks exhibit higher-order dependencies. To address this, various topological models have been employed to describe data in terms of its higher-order relations, including simplicial complexes (Huang et al., 2024), cell complexes (Bodnar et al., 2021), and combinatorial complexes (Hajij et al., 2023). As such, the study of higher-order networks has gained increasing attention for their capacity to capture higher-order interactions (Papamarkou et al., 2024; Zeng et al., 2024a).

Given the broad applicability and theoretical richness of higher-order networks, the following delves deeper into two key frameworks for modelling such interactions: simplicial complexes and cell complexes.

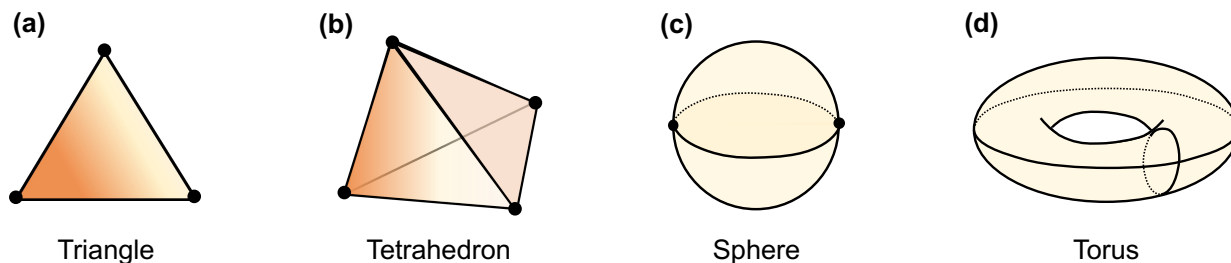


Figure 5. Visual illustration of cell complexes. (a) Triangle. (b) Tetrahedron. (c) Sphere. (d) Torus.

B.1. Simplicial Complexes

Simplicial complexes (SCs) are fundamental concepts in algebraic topology that flexibly subsume pairwise graphs (Hatcher, 2001). Specifically, simplices generalize fundamental geometric structures such as points, lines, triangles, and tetrahedra, enabling the modelling of higher-order interactions in networks. They offer a robust framework for capturing multi-way relationships that extend beyond pairwise connections typically represented in classical networks.

A simplicial complex \mathcal{X} consists of a set of simplices of varying dimensions, including vertices (dimension 0), edges (dimension 1), and triangles (dimension 2).

A d -dimensional simplex is formed by a set of $(d + 1)$ interacting nodes and includes all the subsets of $\delta + 1$ nodes (with $\delta < d$), which are called the δ -dimensional faces of the simplex. A simplicial complex of dimension d is formed by simplices of dimension at most equal to d glued along their faces.

Definition B.1 (Simplicial complexes). A simplicial complex \mathcal{X} is a finite collection of node subsets closed under the operation of taking nonempty subsets, and such a node subset $\sigma \in \mathcal{X}$ is called a simplex.

We can obtain a clique complex, a particular kind of SCs, by extracting all cliques from a given graph and regarding them as simplices. This implies that an empty triangle (owning $[v_1, v_2]$, $[v_1, v_3]$, $[v_2, v_3]$ but without $[v_1, v_2, v_3]$) cannot occur in clique complexes.

B.2. Cell Complexes

Cell complexes generalize simplicial complexes by incorporating generalized building blocks called cells instead of relying solely on simplices (Hatcher, 2001). This broader approach allows for the representation of many-body interactions that do not adhere to the strict requirements of simplicial complexes. For example, a square can be interpreted as a cell of four-body interactions whose faces are just four links. This flexibility is advantageous in scenarios such as social networks, where, for instance, a discussion group might not involve all-to-all pairwise interactions, or in protein interaction networks, where proteins in a complex may not bind pairwise.

Formally, a cell complex is termed regular if each attaching map is a homeomorphism onto the closure of the associated cell's image. Regular cell complexes generalize graphs, simplicial complexes, and polyhedral complexes while retaining many desirable combinatorial and intuitive properties of these simpler structures. In this paper, all cell complexes will be regular and consist of finitely many cells.

As shown in Fig. 5 a and b, triangles and tetrahedrons are two particular types of cell complexes called simplicial complexes (SCs). The only 2-cells they allow are triangle-shaped. The sphere shown in Fig. 5 c is a 2-dimensional cell complex. It is constructed using two 0-cells (*i.e.*, nodes), connected by two 1-cells (*i.e.*, the edges forming the equator). The equator serves as the boundary for two 2-dimensional disks (the hemispheres), which are glued together along the equator to form the sphere. The torus in Fig. 5 d is a 2-dimensional cell complex formed by attaching a single 1-cell to itself in two directions to form the loops of the torus. The resulting structure is then completed by attaching a 2-dimensional disk, forming the surface of the torus. Note that this is just one way to represent the torus as a cell complex, and other decompositions might lead to different numbers of cells and faces.

C. Additional Explanation on Related Works

C.1. Graph Generative Models

Graph generation has been extensively studied, which dates back to the early works of the random network models, such as the Erdős–Rényi (ER) model (Erdős et al., 1960) and the Barabási-Albert (BA) model (Barabási & Albert, 1999). Recent graph generative models make great progress in graph distribution learning by exploiting the capacity of deep neural networks. GraphRNN (You et al., 2018) and GraphVAE (Simonovsky & Komodakis, 2018) adopt sequential strategies to generate nodes and edges. MolGAN (De Cao & Kipf, 2018) integrates generative adversarial networks (GANs) with reinforcement learning objectives to synthesize molecules with desired chemical properties. Shi et al. (2020) generates molecular graphs using a flow-based approach, while GraphDF (Luo et al., 2021) adopts an autoregressive flow-based model with discrete latent variables. Additionally, GraphEBM (Liu et al., 2021) employs an energy-based model for molecular graph generation. However, the end-to-end structure of these methods often makes them more challenging to train compared to diffusion-based generative models.

C.2. Diffusion-based Generative Models

A leap in graph generative models has been marked by the recent progress in diffusion-based generative models (Song et al., 2021). EDP-GNN (Niu et al., 2020) generates the adjacency matrix by learning the score function of the denoising diffusion process, while GDSS (Jo et al., 2022) extends this framework by simultaneously generating node features and an adjacency matrix with a joint score function capturing the node-edge dependency. DiGress (Vignac et al., 2023) addresses the discretization challenge due to Gaussian noise, while CDGS (Huang et al., 2023) designs a conditional diffusion model based on discrete graph structures. GSDM (Luo et al., 2023a) introduces an efficient graph diffusion model driven by low-rank diffusion SDEs on the spectrum of adjacency matrices. GPrinFlowNet (Mo et al., 2024) proposes a semantic-preserving framework based on a low-to-high frequency generation curriculum, where the k -th intermediate generation state corresponds to the k smallest principal components of the adjacency matrices. Despite these advancements, current methods are ineffective at modelling the topological properties of higher-order systems since learning to denoise the noisy samples does not explicitly lead to preserving the intricate structural dependencies required for generating realistic graphs.

C.3. Diffusion Bridge

Several recent works have improved the generative framework of diffusion models by leveraging the diffusion bridge processes, *i.e.*, processes conditioned to the endpoints. Wu et al. (2022) inject physical information into the process by incorporating informative prior to the drift. GLAD (Boget et al., 2024) employs the Brownian bridge on a discrete latent space with endpoints conditioned on data samples. GruM (Jo et al., 2024) utilizes the OU bridge to condition the diffusion endpoint as the weighted mean of all possible final graphs. However, existing methods often overlook or inadvertently disrupt the higher-order topological structures in the graph generation process.

D. Details for Higher-order Guided Generation

D.1. Denoising Network Parametrization

The denoising network in HOG-Diff is a critical component responsible for estimating the score functions required to reverse the diffusion process effectively. The architecture of the proposed denoising network is depicted in Fig. 6. The input \mathbf{A}_t is computed from \mathbf{U}_0 and $\mathbf{\Lambda}_t^{(k)}$ using the relation $\mathbf{A}_t = \mathbf{D}_t^{(k)} - \mathbf{L}_t^{(k)}$, where the Laplacian matrix is given by $\mathbf{L}_t^{(k)} = \mathbf{U}_0 \mathbf{\Lambda}_t^{(k)} \mathbf{U}_0^\top$ and the diagonal degree matrix is given by $\mathbf{D}_t^{(k)} = \text{diag}(\mathbf{L}_t^{(k)})$. To enhance the input to the Attention module, we derive enriched node and edge features using the l -step random walk matrix obtained from the binarized \mathbf{A}_t . Specifically, the arrival probability vector is incorporated as additional node features, while the truncated shortest path distance derived from the same matrix is employed as edge features. Temporal information is integrated into the outputs of the Attention and GCN modules using Feature-wise Linear Modulation (FiLM) (Perez et al., 2018) layers, following sinusoidal position embeddings (Waswani et al., 2017).

A graph processing module is considered permutation invariant if its output remains unchanged under any permutation of its input, formally expressed as $f(\mathbf{G}) = x \iff f(\pi(\mathbf{G})) = x$, where $\pi(\mathbf{G})$ represents a permutation of the input graph \mathbf{G} . It is permutation equivariant when the output undergoes the same permutation as the input, formally defined as $f(\pi(\mathbf{G})) = \pi(f(\mathbf{G}))$. It is worth noting that our denoising network model is permutation equivalent as each model

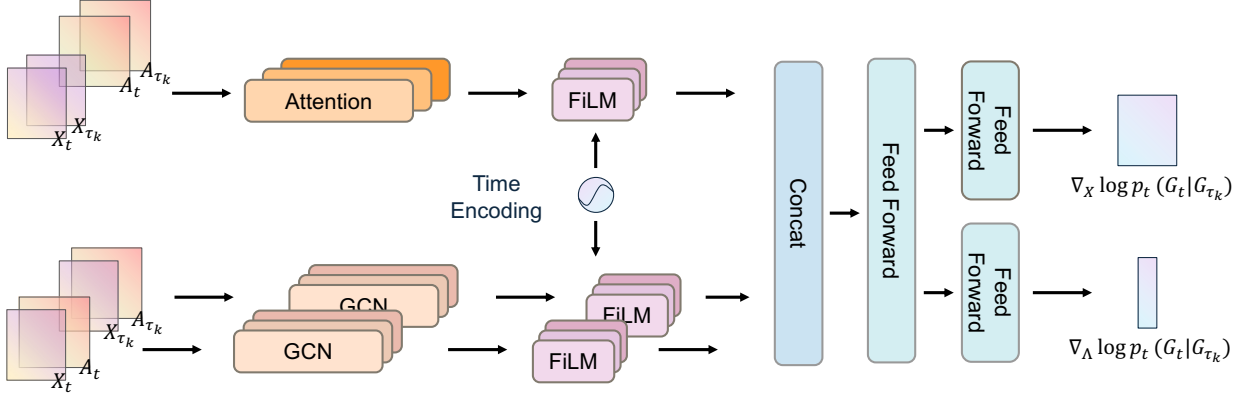


Figure 6. **Denoising Network Architecture of HOG-Diff.** The denoising network integrates GCN and Attention blocks to capture both local and global features, and further incorporates time information through FiLM layers. These enriched outputs are subsequently concatenated and processed by separate feed-forward networks to produce predictions for $\nabla_X \log p_t(G_t | G_{\tau_k})$ and $\nabla_{A_t} \log p_t(G_t | G_{\tau_k})$, respectively.

component avoids any node ordering-dependent operations.

D.2. Training and Sampling Procedure

As shown in Fig. 7, HOG-Diff implements a coarse-to-fine generation curriculum, with the forward diffusion and reverse denoising processes divided into K easy-to-learn subprocesses. Each subprocess is realized using the generalized OU bridge process.

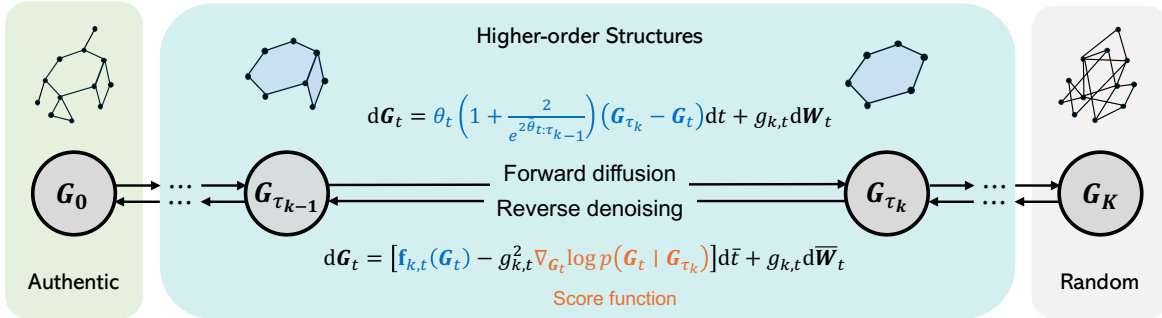


Figure 7. **Illustration of the coarse-to-fine generation process in HOG-Diff using the generalized OU bridge.**

We provide the pseudo-code of the training process in Alg. 1. In our experiments, we adopt a two-step generation process, *i.e.*, $K = 2$. We initialize $\mathcal{S}^{(0)} = \mathbf{G}$; under this specific condition, the cell complex filtering operation returns the input unchanged. The set $\mathcal{S}^{(1)}$ corresponds to the 2-cell complex for molecule generation tasks or the 3-simplicial complex for generic graph generation tasks. We set $\mathcal{S}^{(2)} = \emptyset$, and for this particular case, we define the cell complex filtering function as $\text{CCF}(\mathbf{G}, \emptyset) = \mathcal{N}(\mathbf{0}, \mathbf{I})$.

The pseudo-code of sampling with HOG-Diff is described in Alg. 2. The reverse diffusion processes are divided into K hierarchical time windows, denoted as $\{[\tau_{k-1}, \tau_k]\}_{k=1}^K$, where $0 = \tau_0 < \dots < \tau_{k-1} < \tau_k < \dots < \tau_K = T$. We first initialize the sampling process by drawing samples for $\widehat{\mathbf{X}}_{\tau_K}$ and $\widehat{\mathbf{A}}_{\tau_K}$ from a standard Gaussian distribution, and $\widehat{\mathbf{U}}_0$ is sampled uniformly from the eigenvector matrices of the Laplacian matrix in the training dataset. The reverse-time process starts at τ_K and iteratively updates $\widehat{\mathbf{X}}_t$ and $\widehat{\mathbf{A}}_t$ by solving the reverse-time SDEs with the denoising network $s_{\theta}^{(k)}$. Subsequently, we reconstruct the Laplacian matrix $\widehat{\mathbf{L}}_t$ using the fixed eigenvector matrix $\widehat{\mathbf{U}}_0$ and the updated eigenvalues $\widehat{\mathbf{\Lambda}}_t$. Endpoint of one generation step serves as the starting point for the next process. Finally, after iterating through all diffusion segments, the algorithm returns the final feature matrix $\widehat{\mathbf{X}}_0$ and adjacency matrix $\widehat{\mathbf{A}}_0$, thereby completing the graph generation process.

Algorithm 1 Training Algorithm of HOG-Diff

Input: denoising network $\mathbf{s}_\theta^{(k)}$, authentic graph data $\mathbf{G}_0 = (\mathbf{X}_0, \mathbf{A}_0)$, cell complex list $\{\mathcal{S}^{(0)}, \dots, \mathcal{S}^{(K)}\}$, training epochs M_k .

For the k -th step:

- 1: **for** $m = 1$ **to** M_k **do**
- 2: Sample $\mathbf{G}_0 = (\mathbf{X}_0, \mathbf{A}_0) \sim \mathcal{G}$
- 3: $\mathbf{G}_{\tau_k} \leftarrow \text{CCF}(\mathbf{G}_0, \mathcal{S}^{(k)})$, and $\mathbf{G}_{\tau_{k-1}} \leftarrow \text{CCF}(\mathbf{G}_0, \mathcal{S}^{(k-1)})$ ▷ Cell complex filtering
- 4: $\mathbf{U}_0 \leftarrow \text{EigenVectors}(\mathbf{D}_0 - \mathbf{A}_0)$
- 5: $\mathbf{\Lambda}_{\tau_k} \leftarrow \text{EigenDecomposition}(\mathbf{D}_{\tau_k} - \mathbf{A}_{\tau_k})$
- 6: $\mathbf{\Lambda}_{\tau_{k-1}} \leftarrow \text{EigenDecomposition}(\mathbf{D}_{\tau_{k-1}} - \mathbf{A}_{\tau_{k-1}})$
- 7: Sample $t \sim \text{Unif}([0, \tau_k - \tau_{k-1}])$
- 8: $\mathbf{X}_t^{(k)} \sim p(\mathbf{X}_t | \mathbf{X}_{\tau_{k-1}}, \mathbf{X}_{\tau_k})$ ▷ Eq. (9)
- 9: $\mathbf{\Lambda}_t^{(k)} \sim p(\mathbf{\Lambda}_t | \mathbf{\Lambda}_{\tau_{k-1}}, \mathbf{\Lambda}_{\tau_k})$ ▷ Eq. (9)
- 10: $\mathbf{L}_t^{(k)} \leftarrow \mathbf{U}_0 \mathbf{\Lambda}_t^{(k)} \mathbf{U}_0^\top$
- 11: $\mathbf{A}_t^{(k)} \leftarrow \mathbf{D}_t^{(k)} - \mathbf{L}_t^{(k)}$
- 12: $\ell^{(k)}(\theta) \leftarrow c_1 \|\mathbf{s}_{\theta, \mathbf{X}}^{(k)} - \nabla_{\mathbf{X}} \log p_t(\mathbf{G}_t | \mathbf{G}_{\tau_k})\|^2 + c_2 \|\mathbf{s}_{\theta, \mathbf{\Lambda}}^{(k)} - \nabla_{\mathbf{\Lambda}} \log p_t(\mathbf{G}_t | \mathbf{G}_{\tau_k})\|^2$
- 13: $\theta \leftarrow \text{optimizer}(\ell^{(k)}(\theta))$
- 14: **end for**
- 15: **Return:** $\mathbf{s}_\theta^{(k)}$

Algorithm 2 Sampling Algorithm of HOG-Diff

Input: Trained denoising network $\mathbf{s}_\theta^{(k)}$, diffusion time split $\{\tau_0, \dots, \tau_K\}$, number of sampling steps M_k

- 1: $t \leftarrow \tau_K$
- 2: $\widehat{\mathbf{X}}_{\tau_K} \sim \mathcal{N}(\mathbf{0}, \mathbf{I})$ and $\widehat{\mathbf{\Lambda}}_{\tau_K} \sim \mathcal{N}(\mathbf{0}, \mathbf{I})$
- 3: $\widehat{\mathbf{U}}_0 \sim \text{Unif}(\{\mathbf{U}_0 \triangleq \text{EigenVectors}(\mathbf{L}_0)\})$
- 4: $\widehat{\mathbf{G}}_{\tau_K} \leftarrow (\widehat{\mathbf{X}}_{\tau_K}, \widehat{\mathbf{\Lambda}}_{\tau_K}, \widehat{\mathbf{D}}_{\tau_K} - \widehat{\mathbf{U}}_0 \widehat{\mathbf{\Lambda}}_{\tau_K} \widehat{\mathbf{U}}_0^\top)$
- 5: **for** $k = K$ **to** 1 **do**
- 6: **for** $m = M_k - 1$ **to** 0 **do**
- 7: $\mathbf{S}_X, \mathbf{S}_\Lambda \leftarrow \mathbf{s}_\theta^{(k)}(\widehat{\mathbf{G}}_t, \widehat{\mathbf{G}}_{\tau_k}, t)$
- 8: $\widehat{\mathbf{X}}_t \leftarrow \widehat{\mathbf{X}}_t - \left[\theta_t \left(1 + \frac{2}{e^{2\theta_t \tau_k - 1}} \right) (\widehat{\mathbf{X}}_{\tau_k} - \widehat{\mathbf{X}}_t) - g_{k,t}^2 \mathbf{S}_X \right] \delta t + g_{k,t} \sqrt{\delta t} \mathbf{w}_X, \mathbf{w}_X \sim \mathcal{N}(\mathbf{0}, \mathbf{I})$ ▷ Prediction step: \mathbf{X}
- 9: $\widehat{\mathbf{\Lambda}}_t \leftarrow \widehat{\mathbf{\Lambda}}_t - \left[\theta_t \left(1 + \frac{2}{e^{2\theta_t \tau_k - 1}} \right) (\widehat{\mathbf{\Lambda}}_{\tau_k} - \widehat{\mathbf{\Lambda}}_t) - g_{k,t}^2 \mathbf{S}_\Lambda \right] \delta t + g_{k,t} \sqrt{\delta t} \mathbf{w}_\Lambda, \mathbf{w}_\Lambda \sim \mathcal{N}(\mathbf{0}, \mathbf{I})$ ▷ Prediction step: $\mathbf{\Lambda}$
- 10: $\widehat{\mathbf{L}}_t \leftarrow \widehat{\mathbf{U}}_0 \widehat{\mathbf{\Lambda}}_t \widehat{\mathbf{U}}_0^\top$
- 11: $\widehat{\mathbf{A}}_t \leftarrow \widehat{\mathbf{D}}_t - \widehat{\mathbf{L}}_t$
- 12: $t \leftarrow t - \delta t$
- 13: **end for**
- 14: $\widehat{\mathbf{A}}_{\tau_{k-1}} = \text{quantize}(\widehat{\mathbf{A}}_t)$ ▷ Quantize if necessary
- 15: $\widehat{\mathbf{G}}_{\tau_{k-1}} \leftarrow (\widehat{\mathbf{X}}_t, \widehat{\mathbf{\Lambda}}_t, \widehat{\mathbf{A}}_t)$
- 16: **end for**
- 17: **Return:** $\widehat{\mathbf{X}}_0, \widehat{\mathbf{A}}_0$ ▷ $\tau_0 = 0$

E. Complexity Analysis

When the targeted graph is not in the desired higher-order forms, one should also consider the one-time preprocessing procedure for graph filtering.

Cell filtering can be dramatically accelerated because it avoids explicitly finding all cells and only determines whether nodes and edges belong to a cell. Specifically, the 2-cell filter requires only checking whether each edge belongs to some cycle.

One method to achieve the 2-cell filter is using a depth-first search (DFS). Starting from the adjacency matrix, we temporarily remove the edge (i, j) and initiate a DFS from node i , keeping track of the path length. If the target node j is visited within a path length of l , the edge (i, j) is marked as belonging to a 2-cell of length at most l . In sparse graphs with n nodes and m edges, the time complexity of a single DFS is $\mathcal{O}(m + n)$. With the path length limited to l , the DFS may traverse up to l layers of recursion in the worst case. Therefore, the complexity of a single DFS is $\mathcal{O}(\min(m + n, l \cdot k_{max}))$, where k_{max} is

the maximum degree of the graph. For all m edges, the total complexity is $\mathcal{O}(m \cdot \min(m + n, l \cdot k_{max}))$.

Alternatively, matrix operations can be utilized to accelerate this process. By removing the edge (i, j) from the adjacency matrix A to obtain \bar{A} , the presence of a path of length l between i and j can be determined by checking whether $\bar{A}_{i,j}^l > 0$. This indicates that the edge (i, j) belongs to a 2-cell with a maximum length of $l + 1$. Assuming the graph has n nodes and m edges, the complexity of sparse matrix multiplication is $\mathcal{O}(mn)$. Since l matrix multiplications are required, the total complexity is: $\mathcal{O}(l \cdot m^2 \cdot n)$. While this complexity is theoretically higher than the DFS approach, matrix methods can benefit from significant parallel acceleration on modern hardware, such as GPUs and TPUs. In practice, this makes the matrix-based method competitive, especially for large-scale graphs or cases where l is large.

For simplicial complexes, the number of p -simplices in a graph with n nodes and m edges is upper-bounded by $\mathcal{O}(n^{p-1})$, and they can be enumerated in $\mathcal{O}(a(\mathcal{G})^{p-3} m)$ time (Chiba & Nishizeki, 1985), where $a(\mathcal{G})$ is the arboricity of the graph \mathcal{G} , a measure of graph sparsity. Since arboricity is demonstrated to be at most $\mathcal{O}(m^{1/2})$ and $m \leq n^2$, all p -simplices can thus be listed in $\mathcal{O}(n^{p-3} m)$. Besides, the complexity of finding 2-simplex is estimated to be $\mathcal{O}(\langle k \rangle m)$ with the Bron–Kerbosch algorithm (Bron & Kerbosch, 1973), where $\langle k \rangle$ denotes the average node degree, typically a small value for empirical networks.

F. Experimental Setup

F.1. Computing Resources

In this work, all experiments are conducted using PyTorch on a single NVIDIA L40S GPU with 46 GB memory and AMD EPYC 9374F 32-Core Processor.

F.2. Generic Graph Generation

We follow the experimental and evaluation setting from Jo et al. (2022) with the same train/test split to ensure a fair comparison with baselines. We use node degree and spectral features of the graph Laplacian decomposition as hand-crafted input features.

Tab. 3 summarizes the key characteristics of the datasets utilized in this study. The table outlines the type of dataset, the total number of graphs, and the range of graph sizes ($|V|$). Additionally, it also provides the number of distinct node types and edge types for each dataset. Notably, the synthetic datasets (Community-small and Ego-small) contain relatively small graphs, whereas the molecular datasets (QM9 and ZINC250k) exhibit more diversity in graph size and complexity.

Table 3. Dataset summary.

Dataset	Graph type	#Graphs	#Nodes	Node types	Edge types
Community-small	Synthetic	100	$12 \leq V \leq 20$	1	1
Ego-small	Citation	200	$4 \leq V \leq 18$	1	1
Enzymes	Protein	587	$10 \leq V \leq 125$	1	1
QM9	Molecule	133,885	$1 \leq V \leq 9$	4	3
ZINC250k	Molecule	249,455	$6 \leq V \leq 38$	9	3

F.3. Molecule Generation

Early efforts in molecule generation introduce sequence-based generative models and represent molecules as SMILES strings (Kusner et al., 2017). Nevertheless, this representation frequently encounters challenges related to long dependency modelling and low validity issues, as the SMILES string fails to ensure absolute validity. Therefore, in recent studies, graph representations are more commonly employed for molecule structures where atoms are represented as nodes and chemical bonds as connecting edges (Jo et al., 2022). Consequently, this shift has driven the development of graph-based methodologies for molecule generation, which aim to produce valid, meaningful, and diverse molecules.

In experiments, each molecule is preprocessed into a graph comprising adjacency matrix $\mathbf{A} \in \{0, 1, 2, 3\}^{n \times n}$ and node feature matrix $\mathbf{X} \in \{0, 1\}^{n \times d}$, where n denotes the maximum number of atoms in a molecule of the dataset, and d is the

number of possible atom types. The entries of \mathbf{A} indicate the bond types: 0 for no bound, 1 for the single bond, 2 for the double bond, and 3 for the triple bond. Further, we scale \mathbf{A} with a constant scale of 3 in order to bound the input of the model in the interval $[0, 1]$, and rescale the final sample of the generation process to recover the bond types. Following the standard procedure (Shi et al., 2020; Luo et al., 2021), all molecules are kekulized by the RDKit library (Landrum et al., 2016) with hydrogen atoms removed. In addition, we make use of the valency correction proposed by Zang & Wang (2020). After generating samples by simulating the reverse diffusion process, the adjacency matrix entries are quantized to discrete values 0, 1, 2, 3 by applying value clipping. Specifically, values in $(-\infty, 0.5)$ are mapped to 0, $[0.5, 1.5)$ to 1, $[1.5, 2.5)$ to 2, and $[2.5, +\infty)$ to 3, ensuring the bond types align with their respective categories.

To comprehensively assess the quality of the generated molecules across datasets, we evaluate 10,000 generated samples using several key metrics: validity, validity w/o check, Frechet ChemNet Distance (FCD) (Preuer et al., 2018), Neighborhood Subgraph Pairwise Distance Kernel (NSPDK) MMD (Costa & Grave, 2010), uniqueness, and novelty (Jo et al., 2022). **FCD** quantifies the similarity between generated and test molecules by leveraging the activations of ChemNet’s penultimate layer, accessing the generation quality within the chemical space. In contrast, **NSPDK-MMD** evaluates the generation quality from the graph topology perspective by computing the MMD between the generated and test sets while considering both node and edge features. **Validity** is measured as the fraction of valid molecules to all generated molecules after applying post-processing corrections such as valency adjustments or edge resampling, while **validity w/o correction**, following Jo et al. (2022), computes the fraction of valid molecules before any corrections, providing insight into the intrinsic quality of the generative process. Whether molecules are valid is generally determined by compliance with the valence rules in RDKit (Landrum et al., 2016). **Novelty** assesses the model’s ability to generalize by calculating the percentage of generated graphs that are not subgraphs of the training set, with two graphs considered identical if isomorphic. **Uniqueness** quantifies the diversity of generated molecules as the ratio of unique samples to valid samples, removing duplicates that are subgraph-isomorphic, ensuring variety in the output.

G. Visualization Results

In this section, we additionally provide the visualizations of the generated graphs for both molecule generation tasks and generic graph generation tasks. Figs. 8-12 illustrate non-curated generated samples. HOG-Diff demonstrates the capability to generate high-quality samples that closely resemble the topological properties of empirical data while preserving essential structural details.

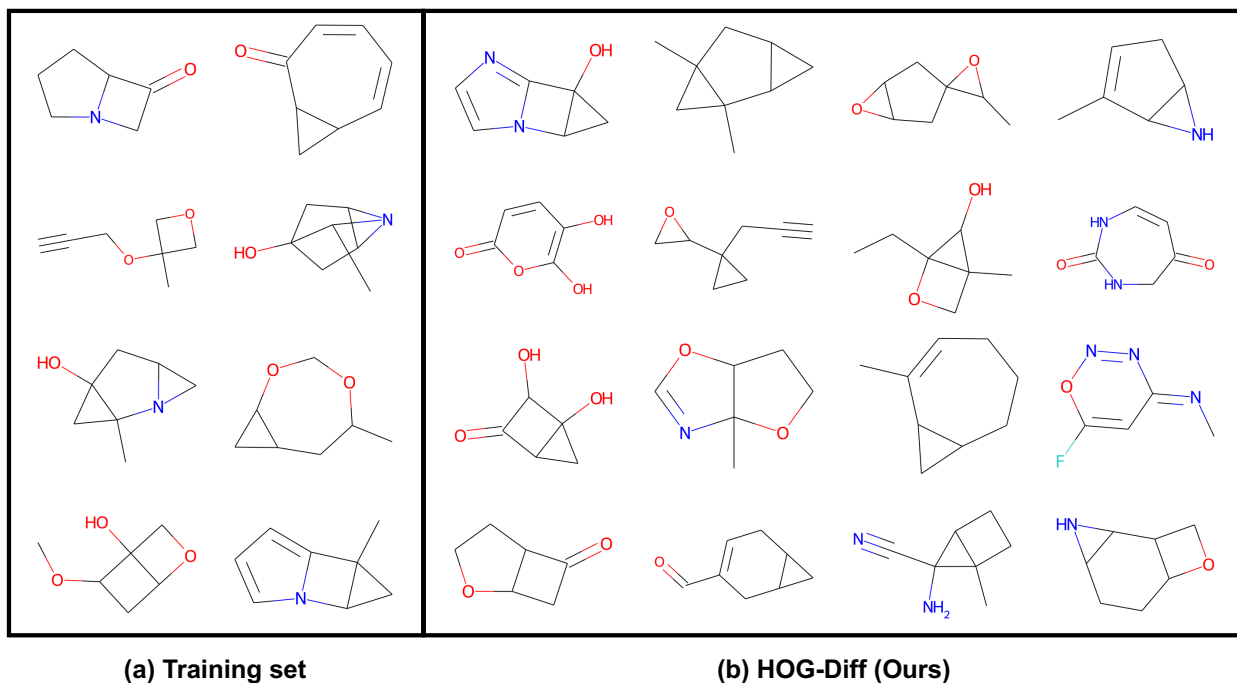


Figure 8. Visualization of random samples taken from the HOG-Diff trained on the QM9 dataset.

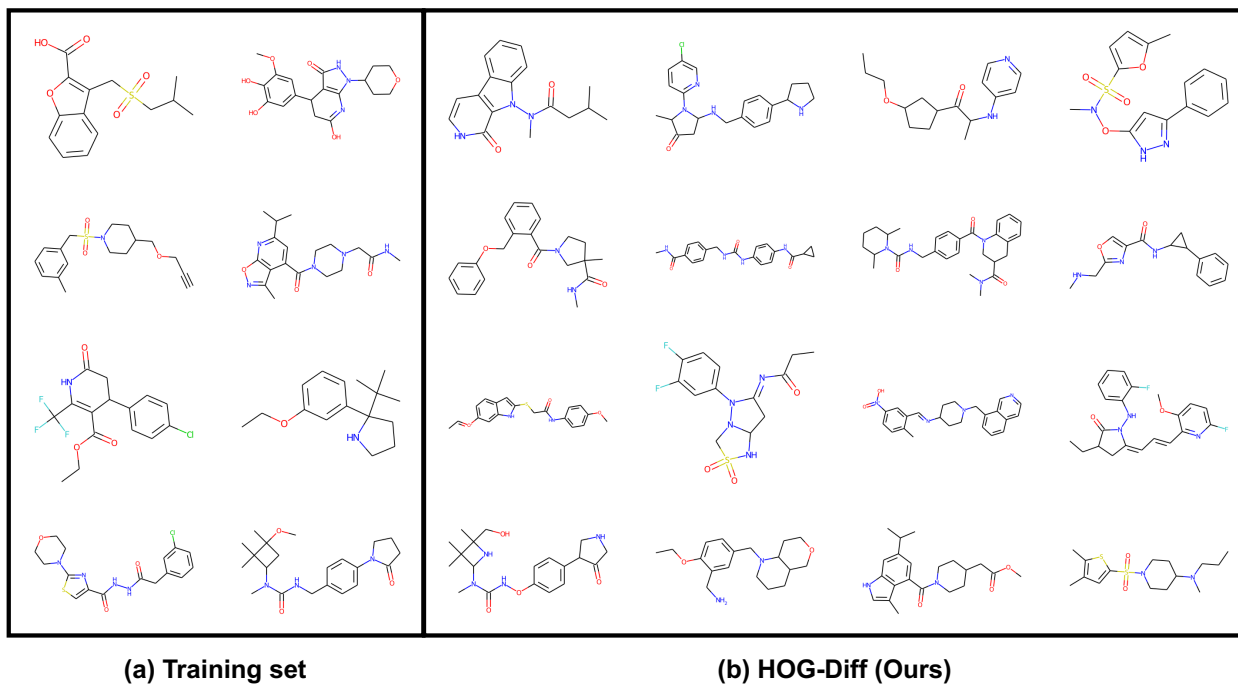


Figure 9. Visualization of random samples taken from the HOG-Diff trained on the Zinc250k dataset.

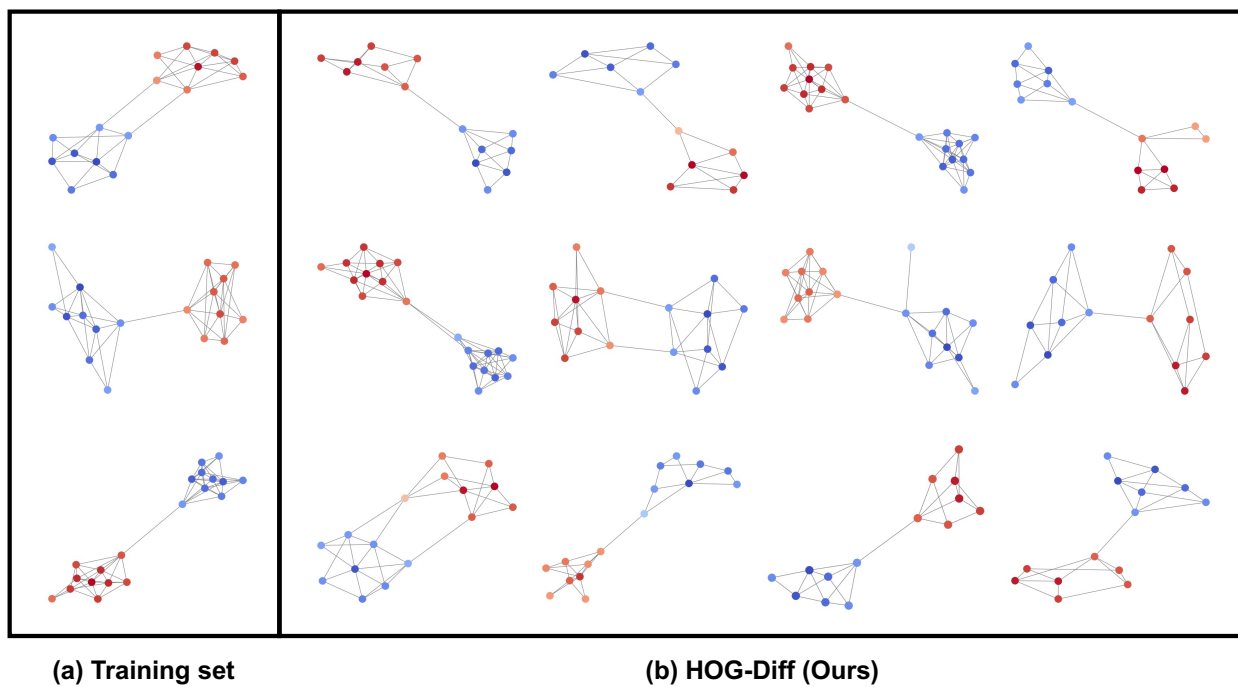


Figure 10. Visual comparison between training set graph samples and generated graph samples produced by HOG-Diff on the Community-small dataset.

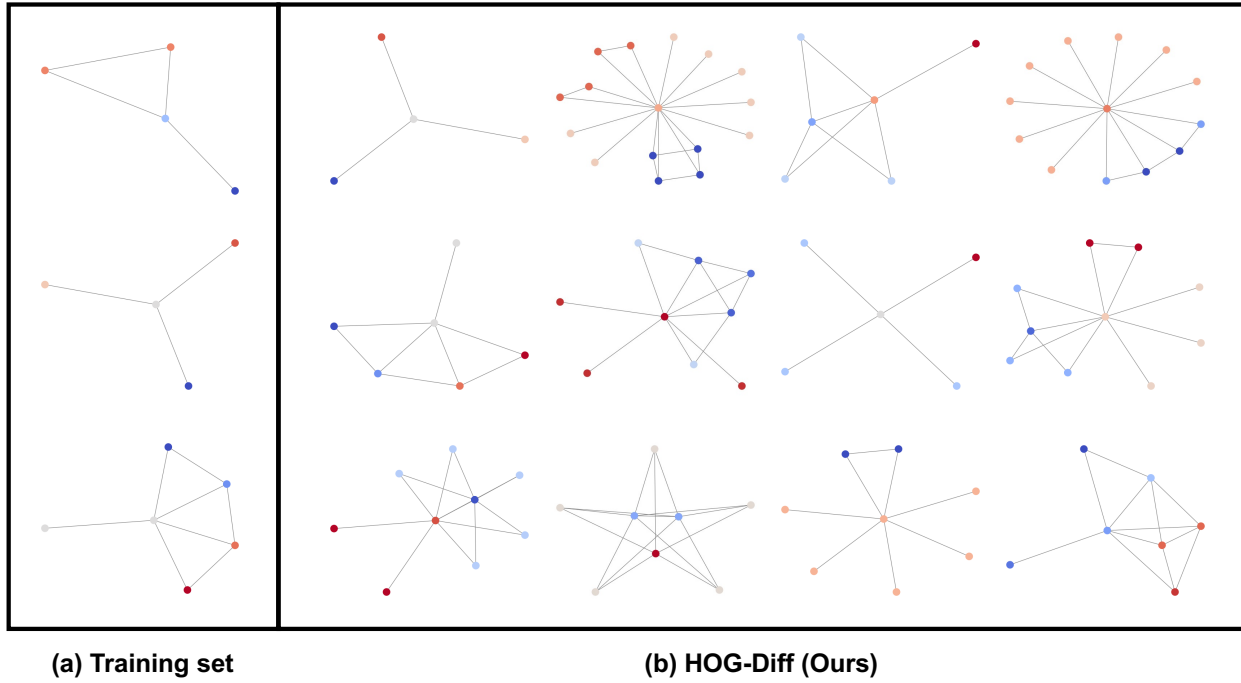


Figure 11. Visual comparison between training set graph samples and generated graph samples produced by HOG-Diff on the Ego-small dataset.

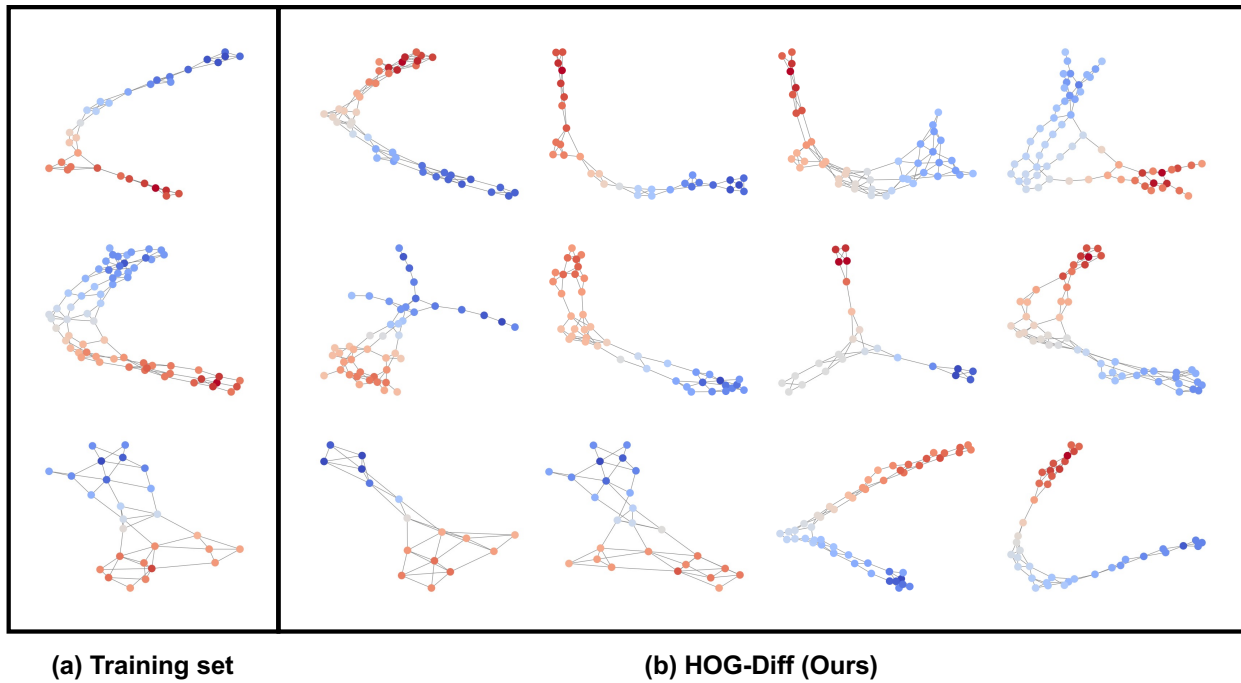


Figure 12. Visual comparison between training set graph samples and generated graph samples produced by HOG-Diff on the Enzymes dataset.